processes

MDPI

Article

Investigating the Characteristics of Two-Phase Flow Using Electrical Capacitance Tomography (ECT) for Three Pipe Orientations

Zeyad Almutairi [1,2,†], Fayez M. Al-Alweet [3,4,*,†], Yusif A. Alghamdi [2,5,*,†], Omar A. Almisned [3] and Othman Y. Alothman [6]

1 Mechanical Engineering Department, King Saud University, P.O. Box 800, Riyadh 11421, Saudi Arabia; zaalmutairi@ksu.edu.sa
2 Sustainable Energy Technologies Center (SET), King Saud University, P.O. Box 800, Riyadh 11421, Saudi Arabia
3 National Center for Oil and Gas Technology, King Abdulaziz City for Science and Technology, P.O. Box 6086, Riyadh 11442, Saudi Arabia; almisned@kacst.edu.sa
4 National Center for Corrosion Technology, King Abdulaziz City for Science and Technology, P.O. Box 6086, Riyadh 11442, Saudi Arabia
5 Deanship of Scientific Research (DSR), King Saud University, Riyadh 11421, Saudi Arabia
6 Department of Chemical Engineering, King Saud University, P.O. Box 800, Riyadh 11421, Saudi Arabia; othman@ksu.edu.sa
* Correspondence: falalweet@kacst.edu.sa (F.M.A.-A.); yalghamdi1@ksu.edu.sa (Y.A.A.); Tel.: +966-11-4814294 (F.M.A.-A.); +966-50-5666977 (Y.A.A.)
† Authors contributed equally.

Received: 24 October 2019; Accepted: 24 December 2019; Published: 2 January 2020

Abstract: Experiments of gas–liquid flow in a circular pipe for horizontal and inclined positions (upward/downward) are reported. The characteristics of two-phase flow in terms of liquid holdup ($\varepsilon_{(L)}$) and induced flow patterns are studied using three experimental techniques; time-averaged $\varepsilon_{(L)}$ from permittivity profiles using electrical capacitance tomography (ECT), instantaneous $\varepsilon_{(L)}$ using two fast-closing valves (TFCV), and high-speed camera images (HSCI) to capture/identify the formed flow patterns. Thus, this experimental setup enables the development of more well-defined flow patterns in gas–liquid two-phase flow and allows for multi-technique verification of the results. Taken from experimental measurements, a model is proposed to predict $\varepsilon_{(L)}$ for high and low situations. The correlations are a function of the hydrodynamic dimensionless quantities which provide hydrodynamic similarity. Regarding different pipe orientations, $\varepsilon_{(L)}$ predictions are comparable to $\varepsilon_{(L)}$ from experimental measurements with accepted accuracy: 88% of the predictions are within ±5–15% and 98% are below ±20%. The correlations also were validated by reported results and against correlations available in the literature and show higher prediction accuracy. It is confirmed that the kinematic similarity which is achieved by the gas–liquid velocity ratios and the inertial forces influence the flow pattern and the liquid holdup.

Keywords: liquid holdup; electrical capacitance tomography; flow pattern; two-phase flow; high speed imaging; intermittent flow pattern

1. Introduction

The Multiphase flow can be defined as the simultaneous existence of dynamic flow in several phases [1]. This occurs in various applications, such as the chemical industry, medical equipment, cooling supercomputers, spacecraft, paper-making plants, boilers and petroleum. Accompanying the

focus on the petroleum industry, it is known that it involves the flow of natural gas, crude oil, water and solids (mud), all of which may be transferred together as multiphase flow in pipes to a refinery [1–3]. As a consequence of the existence of various fluid properties and differences in interfacial properties between them, there will be a wide range of interface configurations and a large number of flow shapes resulting in different flow patterns or regimes [4,5]. Multiphase flow patterns are challenging to identify and a subject of investigation due to their considerable effects on the description and classification of multiphase flows [6].

The most important characteristics of multiphase flow are the flow pattern, $\varepsilon_{(L)}$ (including holdup fluctuations), gas holdup (i.e., void fraction) and pressure drop (including pressure fluctuations). The determination and identification of multiphase flow patterns is of great importance because $\varepsilon_{(L)}$ and pressure drop are highly dependent on the flow pattern. Hence, the flow pattern is a defining feature of multiphase flow. A clear understanding of the flow patterns and the ability to accurately predict the type of flow is extremely important in designing pipelines and in calculating pressure drop and holdup, because each flow pattern has a different effect on these calculations. The prediction and calculation of two-phase flow are highly complex because they involve multiple variables including transfer of momentum, heat and mass, as well as the slippage between the two phases and the presence of interfaces [5–9]. Furthermore, the conduct cross section and configuration, flowrate, direction and inclination significantly affect the flow patterns, pressure drop and $\varepsilon_{(L)}$. Adding to the complexity of multiphase flow, the difference in densities between the components causes slip of the less dense fluids in the pipe [10]. Another influential factor is the inclination angle of the pipe and the direction of flow where both significantly affect the flow patterns and $\varepsilon_{(L)}$.

Generally, the reported flow patterns that are observed in the industrial and research fields include six different flow patterns in an upward inclined flow: dispersed bubbles, plug, elongated bubble, slug, slug churn and annular. Concerning the horizontal pipe condition, adding to the patterns mentioned before, is the existence of a stratified flow pattern. However, for downward pipe flow, and due to gravity, the stratified flow pattern is dominant for macro scale flow conditions [11].

Many instruments and techniques, including visual observation, photography and tomography, have been used in multiphase flow studies to distinguish flow patterns and estimate $\varepsilon_{(L)}$. High-speed camera images (HSCI), acoustic techniques, tomography methods, X-ray imaging, optical fibre probes, hot film anemometry, capacitance sensors, conductance probes and static pressure gauges are the most important methods used today [6,12–20]. Visual observation was formerly used to identify flow patterns at low flow rates only, and is seldom used at all today, having been replaced by HSCI techniques to distinguish flow patterns [21]. As for measuring $\varepsilon_{(L)}$, among the most popular methods that can be employed is the use of two fast closing valves (TFCV) to measure an instantaneous $\varepsilon_{(L)}$. However, lately, tomography technique is extensively utilized because it measures real cross-sectional liquid holdups passing the sensor during a specific time interval. There are many different tomography techniques, such as X-ray and gamma ray nuclear magnetic resonance, acoustic, electrical capacitance and conductance tomography [21–24].

Tomographic techniques are useful to provide images of cross-sectional fluid distribution (internal visualisation), giving a real-time picture of the flow pattern, velocity and concentration of two-phase flow (void fraction and liquid) [15,21,24]. The three main two-phase flow measurement techniques based on electrical properties are electrical capacitance tomography (ECT), electrical resistance tomography (ERT) and electrical inductance tomography (EIT). All these experimental methods generate images, providing cross-sectional distribution information that can yield a real-time picture of the flow, concentration and liquid holdup ($\varepsilon_{(L)}$) in two-phase flows [15,24,25]. Some recent studies showed that the use of the combination between ECT and microwave cavity resonant (MCR) is feasible to measure the liquid holdup and flow pattern in both oil-continuous and water-continuous flow [26].

ECT sensors generally consist of a purpose-built multiplexer, an impedance analyser and a computer for image reconstruction, interpretation and display. The performance of an ECT sensor depends on several parameters, such as the number of electrodes, their dimensions, and type

of electrostatic shielding, axial resolution and its sensitivity [18]. ECT is particularly valuable in characterising multiphase flow for many reasons. First, the fluctuations of the dielectric properties of the gas or liquid within a pipe can be measured and the capacitance of components estimated when they pass through the sensor region. Second, it is non-intrusive to the flow, which means that flow patterns are not disrupted and there will be no erosion of electrodes. ECT sensors usually comprise 8–16 electrodes around the cross section of the pipe, separated from each other by small and equal gaps. The measured values of capacitance will be affected by the geometry of the sensor, the number of electrodes, the configuration of the electrode guard insulators, the fluid temperature inside the pipe and any undesirable stray capacitance, such as that of the cable connecting the sensor to the multiplexer [27–29]. The disadvantages of ECT include the need for a fast data acquisition system, the distortions often affecting reconstructed tomograms and the simultaneous iterative techniques that must be employed to reconstruct an image from permittivity signals [30,31].

Additionally, many theoretical and empirical studies to predict the flow patterns and liquid holdup in two-phase are proposed. Some correlations are developed from data that corresponds to one particular flow pattern (e.g., at intermittent flow, chaotic flow, high or low $\varepsilon_{(L)}$ systems, and slug flow). Annular, stratified and stratified wavy flow patterns are characterized by low solid holdup, and the range of these flow patterns vary between correlations. Spedding and Chen (1984) proposed a correlation to predict the liquid holdup (air/water) for horizontal and vertical pipe with $\varepsilon_{(L)}$ less than 0.20 [32,33], while other correlations could predict $\varepsilon_{(L)}$ for the same flow pattern and similar gas–liquid phases with less than 0.06 for horizontal inclination [33,34]. Slug flow patterns are characterized by relatively higher liquid holdup; this is because the liquid phase occupies a higher fraction of the pipe volume. Many correlations are proposed to predict the liquid holdup for such a flow pattern. The range of this flow pattern varies between $\varepsilon_{(L)}$ values higher than 0.2 (for air/heavy oil for horizontal pipe) and 0.4 (for air/kerosene, air/water, and air/oil for horizontal and upward inclinations), respectively [35–38]. Bestion (1990) proposed a correlation to predict high liquid holdup values for slug flow patterns [38,39]. Similar correlations to predict high liquid holdup also were proposed by Kore et al. (2011) with $\varepsilon_{(L)}$ higher than 0.8 and Al–Safran et al., (2015) with $\varepsilon_{(L)}$ higher than 0.6 using air and high viscosity oil for horizontal pipe [40–42]. Some of the cited correlations depend on the combined effect of the viscous and the inertial forces [33,35,36,40–42], while other correlations proposed by Spedding and Chen (1984), Hamersma and Hart (1987), Bestion (1990) and Ishii (1977) have no viscosity as a variable. Their proposed correlations are influenced by the gas–liquid velocity ratios and the inertial forces [32–34,37–39].

To find the hydrodynamic similarity between different experimental setups, dimensionless numbers such as a Reynold number (*Re*) is usually used; also it is used to scale between multiphase flow systems. The two main forces operating on a gas–liquid multiphase flow system are the inertial and the viscous forces. The relation between these two forces are inherent in a Reynold number (*Re*) [43]. Therefore, in this work a model is proposed which is based on the relation between the liquid holdup as a function of the *Re* of the two phases (i.e., the liquid and the gas). First, this work focuses on examining the influence of the gas–liquid superficial velocities on the flow patterns and on estimating $\varepsilon_{(L)}$ using two eight-electrode ECT sensors, TFCV and a HSCI under three pipe orientation conditions. A multiphase flow rig with adjustable pipe orientations is capable of generating a wide range of multiphase flow patterns is assembled for the current study. During three-stages, the project with the following objectives are investigated: (i) to determine the flow patterns by using two techniques (i.e., a HSCI and electric capacitance tomography), (ii) to measure $\varepsilon_{(L)}$ by means of two techniques (i.e., TFCV and ECT sensors), and (iii) to develop an empirical correlation that predicts $\varepsilon_{(L)}$ with high accuracy as a function of the hydrodynamics non-dimensional properties of multiphase flow in terms of the *Re* of the gas and the liquid phases. The proposed model is validated by two independent measuring techniques which is rarely available in the literature. It also was validated by the extractable results from the literature.

2. Experimental Apparatus

The experimental setup comprises of a flow rig, an ECT capacitance sensor, and high-speed imaging system, schematically illustrated in Figure 1. The flow rig consists of a large reservoir, a gear pump, a compressor, gas and oil flow sensors, TFCV and the pipe network. A 6 m-long test section of the pipe can be adjusted to a selected angle using a swing table. This test section has TFCV (SV6007-NO model, Omega, Norwalk, CT, USA), one at the inlet and the other at the outlet. An electrical delay circuit is used to postpone pump and compressor turn-off for 0.9 s after the valves on the test section are closed to measure $\varepsilon_{(L)}$. The test section is made of a transparent acrylic with an inner diameter of d_{in} = 3.6 cm, allowing visual observation of the creation and development of the flow patterns. Toward the end of the experimental pipe section, a viewing box made of glass encloses a small portion of the pipe, as shown in Figure 2a. This box is filled with water to reduce the lensing effect of the pipe when examining the flow patterns with the high-speed camera.

Mineral oil ($\rho_{(L)}$ = 850 kg/m^3) at room temperature is pumped into the flow loop, which is designed as an open recycling system to ensure an appropriate phase mixing and to allow various flow patterns to be developed. Compressed air ($\rho_{(G)}$ = 1.204 kg/m^3) at room temperature is injected into the flow rig using an in-house gas/liquid mixer. The mass flow rate of air is controlled and measured by two instruments: (a) float ball and (b) mass flow meter (FMA 1700/1800 model, Omega, Norwalk, CT, USA). The oil flow rate is controlled by varying the speed of the pump motor and is measured with a turbine flow meter (A10GMN100NA1, GPI)).

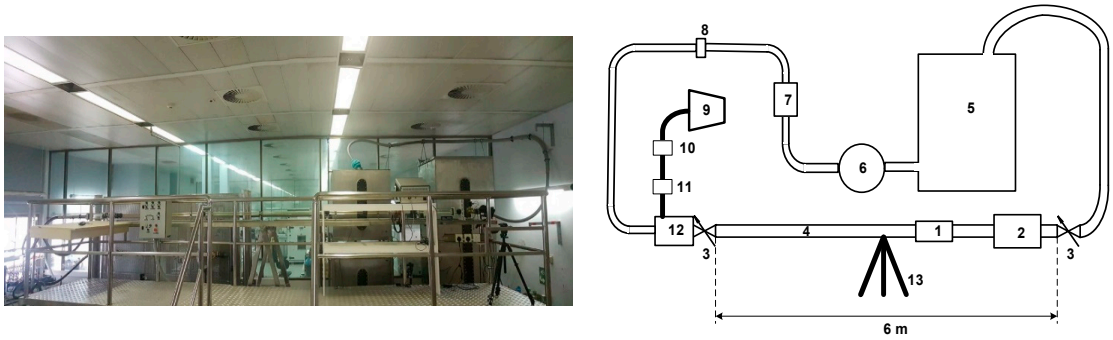

(**a**) (**b**)

Figure 1. (**a**) Photograph of the flow rig. (**b**) Schematic illustration of the test rig used in the current work. The numbered items are: 1—ECT capacitance sensor, 2—viewing box, 3—fast-closing valves, 4—transparent 36 mm inner diameter polycarbonate pipe, 5—mineral oil reservoir, 6—gear pump, 7—flow rotameter, 8—turbine flow meter, 9—air compressor, 10—float flow meter, 11—gas mass flow meter, 12—mixing chamber, 13—swing table for pipe support.

The ECT system (PLT model, Process Tomography Ltd., Wilmslow, Cheshire, UK) is located 4.5 m from the flow mixer and uses a TFLR5000 data acquisition system. The system consists of two sensors with 42 mm separating the middle plane of each centre plane (i.e., copper screen in Figure 2a). Each plate has 8 electrodes spaced at 40 mm intervals along the axial length of the pipe and 47.6 mm around its perimeter. Eight driven guard electrodes of 25 mm axial length are located on each sensor behind the capacitance measurement electrodes. The driven guard electrodes and the sensor electrodes are enclosed within an earthed cylindrical screen, fabricated from copper sheet formed into an open cylinder, which is held in place by a set of circumferential steel bands. The steel bands compress a set of radial clamps (attached to the end rings) onto the electrode foil of the sensor and the tube, as well as securing the outer screen, as shown in Figure 2b. A schematic illustration cross-section of the sensor is shown in Figure 2c. The 8 electrode twin plane sensor is mounted on a 40 mm OD Perspex tube with a wall thickness of 2 mm (i.e., inner diameter 36 mm). The measurement electrodes (E1–E8) are spaced on 45 degrees, centers at an effective radius of 20.5 mm. Each electrode's circumferential arc length is 14 mm, which corresponds to a subtended angle of about 19.5 degrees. The electrodes are

separated by an insulating gap of circumferential length 0.5 degrees and an axial guard electrode of circumferential length 1 mm, corresponding to a subtended angle of approximately 2.8 degrees. Radial metal screening fins (i.e., S in Figure 2c) of radial height 10 mm are attached to the axial guard tracks.

(**a**)

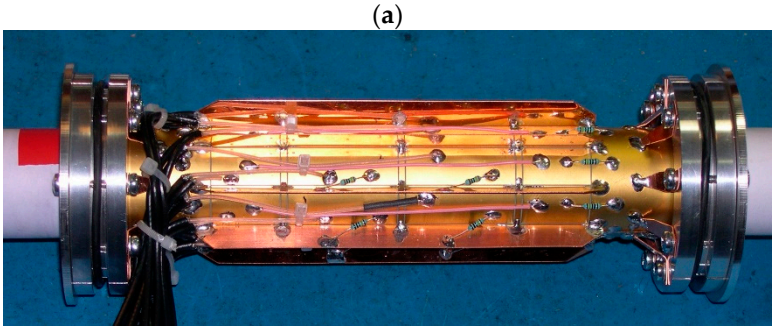

(**b**)

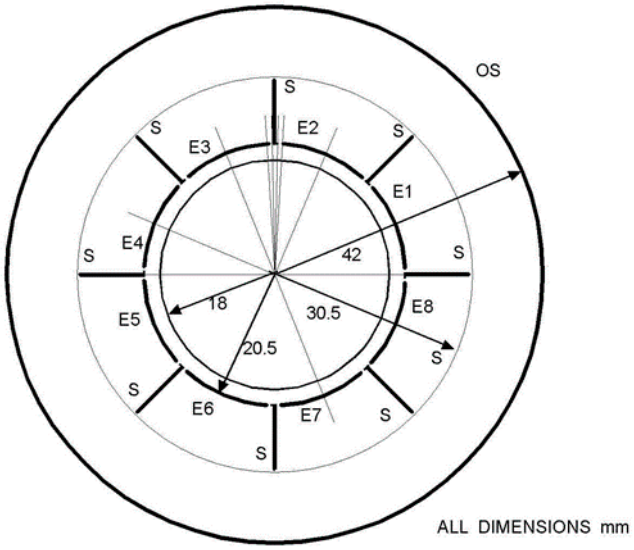

(**c**)

Figure 2. Photographic view (**a**) the transparent rectangular box and ECT sensor, (**b**) ECT equipment used in the experiments, and (**c**) schematic illustration of the ECT sensor cross-section.

The data from the capacitance sensor is recorded using the ECT32v3 software (Process Tomography Ltd., Wilmslow, Cheshire, UK). It is worth noting that one of the purposes of using two sensors is to estimate the velocity fields and then the volume flowrate with cross correlation algorithms. However, in this work more attention is directed toward determining and measuring $\varepsilon_{(L)}$. The high-speed camera (CR4000 × 2, Optronis GmbH, Kehl, DE) captures 500 frames per second for 15–30 s at a full resolution of 4 megapixels and can achieve higher acquisition rates for cropped fields of view. The camera has an F mount with a Nikon 50 mm f/1.8D attached to it. The viewing box is backward illuminated with an LED assembly that provides a uniform and stable light intensity when using the high-speed camera.

Experimental Procedure

The main sensor in the current work was the ECT sensor. The typical operation was as follows. One electrode served as a source for the electrical signal and the other electrodes recorded square wave voltage signals in the MHz range, corresponding to the passage of electrical fields across the inside pipe. This step took around 25 µs and was repeated ultra-rapidly for each of the seven electrodes. Thus, the electric field relations between the electrodes corresponded to the medium present in the pipe. When two materials with different permittivity passed through the pipe, they affected the pathways of the electric field. Therefore, since in a single cross-sectional permittivity measurement each electrode was used sequentially as a source one at a time, the full permittivity map in the plane of measurement was calculated.

The signal recorded by the ECT sensor was calibrated by taking background signals for both the gas phase, which had a lower permittivity (air permittivity is one), and the oil phase, which had a higher permittivity (oil permittivity is $E = 2.1$). This step was crucial in inferring the liquid phases measured with linear back projection (LBP). The values of $\varepsilon_{(L)}$ were calculated from the ECT signals using the ECT32v3 commercial software that was used to control the sensor. The raw data recorded by the ECT sensors represented the permittivity distribution in the measurement plane of the pipe cross-section area for the two fluid phases (i.e., gas and liquid). The data were then analyzed with knowing the reference matrix and background signals recorded during the calibration step. Hence, the resulting image was a cross-sectional representation of the volumetric region passing through the measurement sensor. Typical images were reconstructed with 32×32 pixel^2. This gave a resolution of 1.25 mm^2 that was identified in the smallest interrogation area.

During a typical experiment, the flow conditions were set to desired flow rates and a waiting period of at least 5 minutes was allowed for the flow patterns to stabilize, which was confirmed by naked eye observation of the flow patterns. The camera and ECT sensor were then turned on to capture the video file and capacitance data for the flow condition being tested. The ECT data was taken for around 60 s. The camera acquisition settings were varied between 60 and 500 frames per second, according to the speed of the flow patterns.

Occurring at the end of the data recording, the TFCV were closed immediately, thus capturing an instantaneous flow condition in the 6 m straight section of pipe. The volume of air inside this section was found by tilting it and measuring the length of the air inside the pipe. Using this measurement, $\varepsilon_{(L)}$ was then calculated. The height measurements were carried out with an accuracy of ±1 mm. Thus, the error associated in measuring the length of the air section and, therefore, obtaining $\varepsilon_{(L)}$ was estimated to be around ±7.2% (with 10% deviation) of the measured $\varepsilon_{(L)}$ [44].

The above procedure was performed for all test conditions in Table A1 (i.e., in Appendix A). Thus, in this work, three pipe positions were studied: horizontal, inclined upward at 9° and inclined downward at −9°. Considering economical purposes in the oil and gas industry, the pipeline inclinations should not be greater than 25° [45]. Additionally, in the oil and gas industry at the gathering stations and the plain regions (i.e., at the upstream or downstream) most pipelines are positioned in the horizontal/near-horizontal inclination [45,46]. The selected inclinations for this study i.e., 0°, +9°, −9° fall between a generally used range of operating conditions in this sector and by many researchers [45,47–49]. Regarding each position, the flowrate ratio between the gas (i.e., Compressed Air) and oil (i.e., Mineral oil) were modified from 0.77 to about 34. Where three oil flow rate conditions were examined, that is 1.34×10^{-4} m^3/s, 2.70×10^{-4} m^3/s, and 5.20×10^{-4} m^3/s (i.e., 0.135 m/s, 0.276 m/s, and 0.51 m/s), the gas flow rate was varied and increased gradually from 4.17×10^{-4} m^3/s to 5.10×10^{-3} m^3/s (i.e., 0.4 m/s to 5 m/s). These variations allowed for various $\varepsilon_{(L)}$ to be developed and different corresponding flow patterns to be generated in the test pipe. Each value of $\varepsilon_{(L)}$, was obtained simultaneously from TFCV and capacitance sensors where, at each reading, the flow pattern was identified by observation of the transparent pipe, either by eye at low velocities or by HSCI at high velocities.

3. Correlation Development

The holdup in a multiphase system (i.e., gas–liquid, liquid–liquid or gas–solid) is affected by many factors including gas/liquid/solid superficial velocities, liquid/gas/solid densities and viscosities, the conduit dimension and inclinations [25,32–43,50–53]. Concerning a gas-liquid multiphase flow in a pipe, the holdup is a function of the following factors [43]:

$$\varepsilon_{(L)} = f(\rho_{(L)}, \rho_{(G)}, \mu_{(L)}, \mu_{(G)}, u_{(L)}, u_{(G)}, d_{in}, \theta) \quad (1)$$

where $\rho_{(L)}$, $\rho_{(G)}$, $\mu_{(L)}$ $\mu_{(G)}$, $u_{(L)}$ and $u_{(G)}$ are gas–liquid densities, viscosities and superficial velocities, respectively,d_{in} is the internal pipe diameter and θ is the inclination angle. It is conceptually accepted that the two main forces operating on gas–liquid multiphase flow systems are the inertial and the viscous forces. The relation between these two forces can be shown in Reynold number (Re) as follows [43],

$$Re = \frac{\rho u d_{in}}{\mu} \quad (2)$$

Seen in a gas–liquid multiphase flow are two Re numbers, which can be identified as one for the gas phase and the other for the liquid phase:

$$Re_{(G)} = \frac{\rho_{(G)} u_{(G)} d_{in}}{\mu_{(G)}} \quad (3)$$

$$Re_{(L)} = \frac{\rho_{(L)} u_{(L)} d_{in}}{\mu_{(L)}} \quad (4)$$

Therefore, Reynold numbers can provide a platform for developing an $\varepsilon_{(L)}$ correlation with greater accuracy and broader applicability to systems operating under different operating conditions over the entire flow regimes. This is because it is usually used to provide a hydrodynamic similarity between different systems [43]. Considering experimental observations in this work and others [54–56], $\varepsilon_{(L)}$ takes a non-linear form and, hence, the relation between $\varepsilon_{(L)}$ and Reynold numbers can be expressed as follows:

$$\varepsilon_{(L)} = a\left[Re_{(G)} / Re_{(L)}\right]^b \quad (5)$$

or rewritten as,

$$\varepsilon_{(L)} = a\left[\frac{\rho_{(G)} u_{(G)} d_{in}}{\mu_{(G)}} / \frac{\rho_{(L)} u_{(L)} d_{in}}{\mu_{(L)}}\right]^b \quad (6)$$

When the velocity, density, viscosity and diameter ratios are grouped together, and since the pipe diameter is constant for any operating condition (i.e., d_{in}/d_{in} = 1), Equation (6) can be simplified to:

$$\varepsilon_{(L)} = a\left[\left(\frac{u_{(G)}}{u_{(L)}}\right)\left(\frac{\rho_{(G)}}{\rho_{(L)}}\right)\left(\frac{\mu_{(L)}}{\mu_{(G)}}\right)\right]^b \quad (7)$$

where, the coefficient a and the exponent b are non-linear regression constants.

To determine the values of the coefficient and the exponent in Equation (7), which gave the best fit between the dimensionless quantities and the experimental data, a step-by-step nonlinear least squares regression analysis was carried out [57]. This was done by conducting 3 steps of the nonlinear minimum square regression analysis to obtain the values of the coefficient and exponent (i.e., a and b), which shows the significance of each individual dimensionless quantity to yield the highest values of the statistical number (R^2) which measures the accuracy of the fitted regression line, adjusted R^2 and the minimum standard deviation between the observed and predicted values. Additionally, to broaden the applicability of the proposed correlation, different data from different experimental setups at various operating conditions (i.e., temperature, pressure, and liquid medium e.g., Kerosene and water)

were considered [51,53]. Thus, the total data points used to develop this empirical correlation were about 310. Figure 3 shows a plot of the dimensionless numbers in Equation (7) and the experimental $\varepsilon_{(L)}$. The data collected and used to develop the correlation consisted of data from systems that operate at high and low $\varepsilon_{(L)}$. Attempts were made to correlate them together to one correlation, however, there was a transition region which increased the prediction uncertainty and error (it will be explained later), thus, two separate correlations were developed.

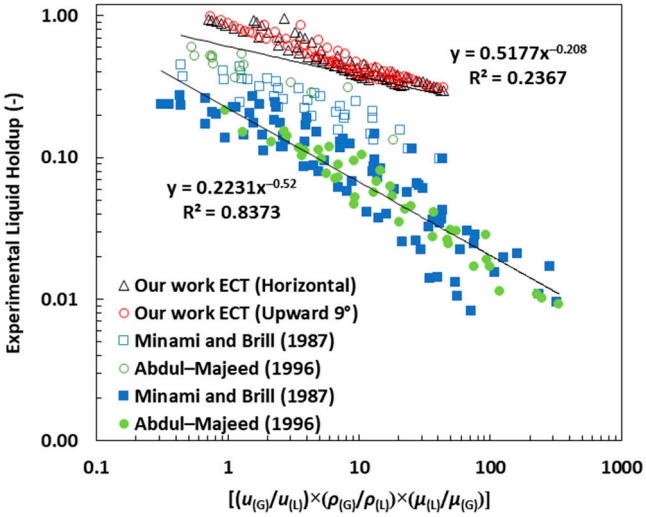

Figure 3. The experimental $\varepsilon_{(L)}$ expressed as a function of the dimensionless quantities in Equation (7): logarithmic comparison of $\varepsilon_{(L)}$ (i.e., 310 data points) obtained from this work, [51,53].

Also, Figure 3 shows the unfitted power–law relationship between the experimental values of $\varepsilon_{(L)}$ and the dimensionless numbers that were used to correlate the operation conditions. Accordingly, the resultant correlations can be expressed as:

$$\varepsilon_{(L)} = 0.5177\left[\left(\frac{u_{(G)}}{u_{(L)}}\right)\left(\frac{\rho_{(G)}}{\rho_{(L)}}\right)\left(\frac{\mu_{(L)}}{\mu_{(G)}}\right)\right]^{-0.208} \quad (8)$$

$$\varepsilon_{(L)} = 0.2231\left[\left(\frac{u_{(G)}}{u_{(L)}}\right)\left(\frac{\rho_{(G)}}{\rho_{(L)}}\right)\left(\frac{\mu_{(L)}}{\mu_{(G)}}\right)\right]^{-0.52} \quad (9)$$

where Equations (8) and (9) are for high and low $\varepsilon_{(L)}$, respectively.

Statistical analysis was conducted to determine the significance of each ratio in Equations (8) and (9) (i.e., the velocity ratio, density ratio and the viscosity ratio). Stepwise non-linear regression was conducted, and it was found that the velocity ratio was the most significant ratio in the relation with $\varepsilon_{(L)}$, as shown in Figure 4a. The obtained individual exponent for the velocity ratios ratio $(u_{(G)}/u_{(L)})$ were −0.29 (for high $\varepsilon_{(L)}$) and −0.0913 (for law $\varepsilon_{(L)}$). The significance can be attributed to the formation of different flow regimes/patterns that can be identified by their corresponding $\varepsilon_{(L)}$ value. Therefore, these flow patterns are largely influenced by the gas–liquid velocities ratio. Thus, to be able to extend the application of the proposed correlation, the kinematic similarity is achieved by the gas–liquid velocity ratio [43]. Additionally, Figure 4b shows the result obtained from the individual exponent for the density ratios $(\rho_{(G)}/\rho_{(L)})^{-0.19}$ for high $\varepsilon_{(L)}$ and $(\rho_{(G)}/\rho_{(L)})^{-0.573}$ for low $\varepsilon_{(L)}$. The resultant factor is large, which will affect the prediction of $\varepsilon_{(L)}$, therefore, considering the density ratio in the regression analysis increased the predictability of the correlation in terms of R^2. However, for the viscosity ratio, the individual exponent obtained was −0.0057 (for high $\varepsilon_{(L)}$) and −0.048 (for low $\varepsilon_{(L)}$). It can be seen that, for all the experimental data the values of $(\mu_{(L)}/\mu_{(G)})^{-0.0057}$ and $(\mu_{(L)}/\mu_{(G)})^{-0.048}$ were between 0.80–1, respectively, as shown in Figure 4c. Farokhpoor et al., (2020) showed a similar conclusion

where the velocity and density ratios influenced the flow pattern and the liquid holdup, while the viscosity ratio had little influence [43].

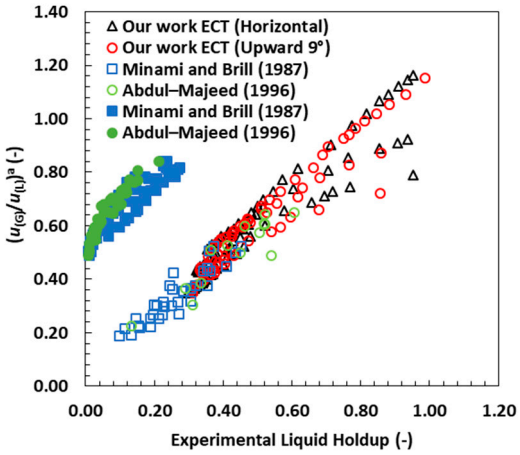

(**a**)

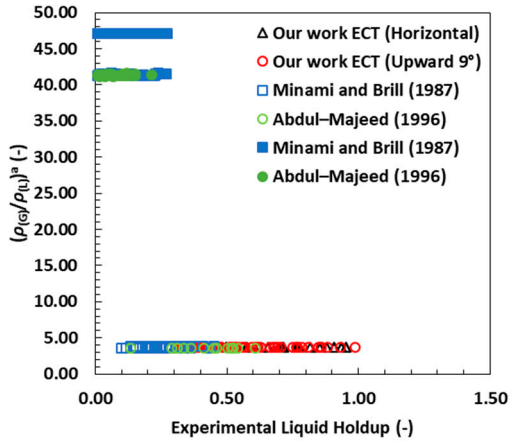

(**b**)

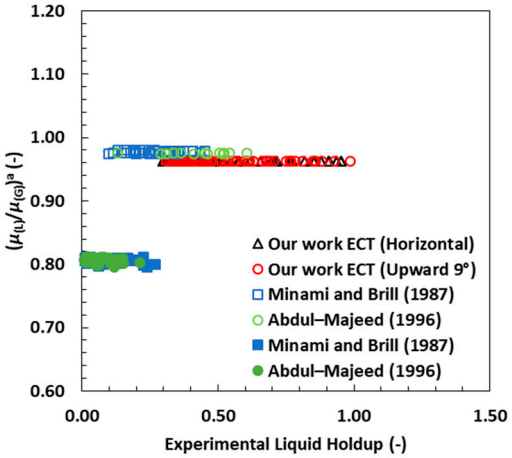

(**c**)

Figure 4. Variation of values of (**a**) $(u_{(G)}/u_{(L)})^{-0.29}$ and $(u_{(G)}/u_{(L)})^{-0.0913}$, (**b**) $(\rho_{(G)}/\rho_{(L)})^{-0.19}$ and $(\rho_{(G)}/\rho_{(L)})^{-0.573}$, and (**c**) $(\mu_{(L)}/\mu_{(G)})^{-0.0057}$ and $(\mu_{(L)}/\mu_{(G)})^{-0.048}$ as a function of $\varepsilon_{(L)}$.

Since the factor obtained from the viscosity ratio was very small, Equation (7) can be further simplified to:

$$\varepsilon_{(L)} = a\left[\left(\frac{u_{(G)}}{u_{(L)}}\right)\left(\frac{\rho_{(G)}}{\rho_{(L)}}\right)\right]^{b} \tag{10}$$

The developed correlation based on the relation obtained in Equation (10) showed a better and very well-fitted power–law relationship between the experiment $\varepsilon_{(L)}$ and the dimensionless quantity, as shown in Figure 5.

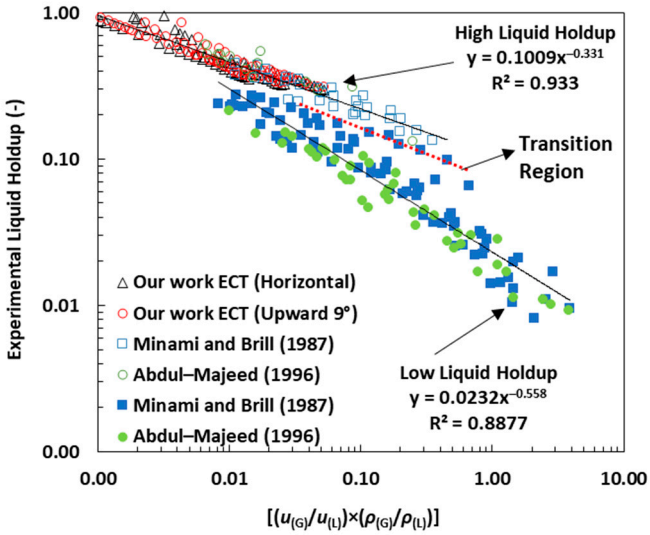

Figure 5. The experimental $\varepsilon_{(L)}$ expressed as a function of the dimensionless quantities in Equation (10): logarithmic comparison of $\varepsilon_{(L)}$ (i.e., 310 data points) obtained from this work, [51,53].

Accordingly, the resultant correlation can be expressed as:

$$\varepsilon_{(L)} = 0.1009\left[\left(\frac{u_{(G)}}{u_{(L)}}\right)\left(\frac{\rho_{(G)}}{\rho_{(L)}}\right)\right]^{-0.331} \tag{11}$$

$$\varepsilon_{(L)} = 0.0232\left[\left(\frac{u_{(G)}}{u_{(L)}}\right)\left(\frac{\rho_{(G)}}{\rho_{(L)}}\right)\right]^{-0.558} \tag{12}$$

where Equations (11) and (12) represent high and low $\varepsilon_{(L)}$, respectively. The proposed empirical correlations were developed for the following ranges, Equation (11) for $u_{(G)}$ = 0.105–5.20 m/s, $u_{(L)}$ = 0.0018–0.512 m/s, $u_{(G)}/u_{(L)}$ = 0.60–301.2, and $\rho_{(G)}/\rho_{(L)}$ = 0.0012–0.0015, and Equation (12) for $u_{(G)}$ = 1.56–16.6 m/s, $u_{(L)}$ = 0.00186–0.95 m/s, $u_{(G)}/u_{(L)}$ = 6.55–2564, and $\rho_{(G)}/\rho_{(L)}$ = 0.0012–0.0015.

4. Results and Discussions

4.1. Gas–Liquid Flow Pattern Characteristics Using ECT

The ECT technique is a soft field method for the reconstruction of the permittivity patterns of liquids at the volume of interest. During the current work, the ECT was used to estimate $\varepsilon_{(L)}$ and, later, it was compared to the instantaneous $\varepsilon_{(L)}$ that was caught with TFCV. Iteration algorithms to improve the image quality can be used, however, the scope of the current work focused on examining flow patterns, in particular $\varepsilon_{(L)}$, and providing a correlation for gas–liquid two phase flow in circular conduits. The values of $\varepsilon_{(L)}$ are averaged values of all the instantaneous ECT images, which were taken as continuous measurements for 60 s. The averaging was done according to this duration by the

ECT software. The color scale beside the ECT images in Figure 6 give clear indication of the liquid phase, gas phase and the gas–liquid interface.

The experimental recordings from the ECT sensors were analysed according to the procedure presented in the experimental section. To avoid the repetition in discussing the ECT images, a sample of the ECT images were selected and discussed here in detail. Typical images presenting phase concentration colour coding are blue for the lower permittivity fluid (gas phase), red for the higher permittivity fluid (oil phase), and green for the interface between two phases, as shown in Figure 6. Found at low superficial gas velocity that was in the plug flow pattern (i.e., for upward inclinations), the gas phase appeared as cap-bubbles which alternated with liquid at the top of the pipe, with an average $\varepsilon_{(L)}$ of 0.933. Initially, the pipe was full of liquid (high permittivity fluid) as shown in Figure 6a. As the leading face of the bubble (plug flow pattern) approached the capacitance sensor and the nose of the bubble was just entering the screen of the capacitance, the effect of the bubble's (low permittivity air) was observed on the image, as in Figure 6b, which shows the gas phase in the middle of the image surrounded by a liquid phase. Figure 6c shows the bubble (gas phase) when it occupied the central section of the pipe and passed in the middle of the sensor. The bubble became bigger than what was seen in Figure 6b, as a result of the changing size of bubbles crossing the sensor. Figure 6d shows the image captured by the ECT as the bubble trail was leaving the screen of the capacitance sensor and the liquid was starting to fill the pipe again. This cycle was repeated as the next bubble passed the capacitance sensor screen. Such repeated cycles of this flow pattern (i.e., plug) led to intense fluctuation of $\varepsilon_{(L)}$.

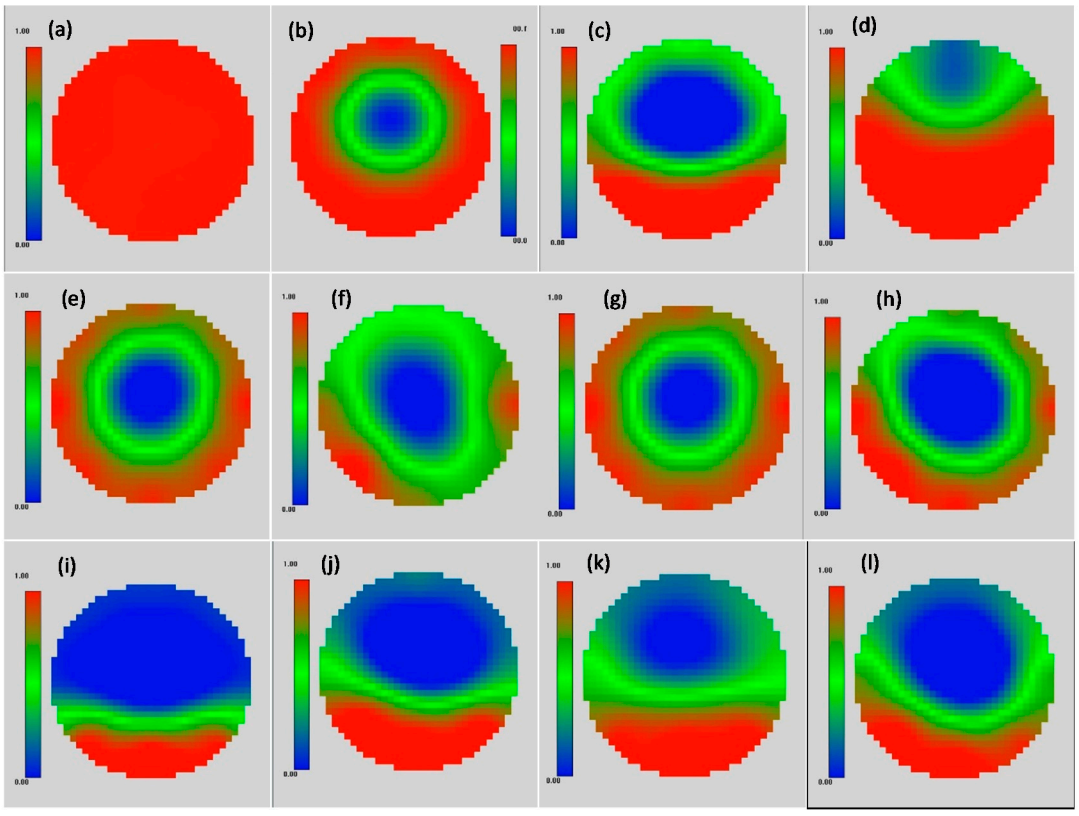

Figure 6. Evolution of fluid permittivity distributions calculated from electrical potential distributions for the sensor measurement cross-section of an area fraction captured by the ECT sensor for a typical experiment (**a**–**d**) corresponding to upward plug flow pattern at $u_{(L)}$ = 0.506 m/s and $u_{(G)}$ = 0.377 m/s, (**e**–**h**) corresponding to upward annular flow pattern at $u_{(L)}$ = 0.1333 m/s and $u_{(G)}$ = 5 m/s, and (**i**–**l**) the corresponding to horizontal stratified pattern at $u_{(L)}$ = 0.137 m/s and $u_{(G)}$ = 4.47 m/s, (Red = liquid phase, Blue = gas phase, and Green = interface between two phases).

Figure 6e–h, shows an example of a volumetric profile of an upward inclination flow condition, where there is formation of oil film around the pipe wall, while the middle of the pipe is occupied by the air. The estimated averaged liquid volume fraction for this condition is 0.310. Regarding annular flow patterns, the gas phase flowed along the core of the pipe while the liquid phase flowed along and adjacent to the pipe wall as a wavy liquid film. The two phases were always separated, and the thickness of the oil film fluctuated continuously. The oil film was usually thicker at the bottom than that at the top of the pipe, as shown in Figure 6e, due to the gravity effect. This film thickness could not stay uniform with respect to time, as waves of oil were swept around the pipe periphery. Thus, the electrical potential distribution fluctuated in accordance with the wavy interface of the film, as shown in Figure 6f–h. The distribution of the annular oil film around the pipe had a major effect on the electrical field distribution inside the capacitance sensor. Figure 6e–h shows the fluctuations in the electrical field distribution, which indicate the variations in oil film thickness: the red colour indicates thicker oil film, which sometimes appears around the pipe wall as shown in Figure 6e,g; the blue colour indicates the gas phase, which is always seen in the core of the pipe; green regions indicate the interface between the oil phase and gas phase. When the green colour touches the pipe wall and is around the pipe wall, it means thin oil film as shown in Figure 6f,h. These images will be repeated, as the annular flow pattern was seen in the test section and the capacitance sensor was used to detect this flow pattern.

Stratified flow (i.e., for the horizontal case) occurred when liquid flowed at the bottom of the pipe and the gas phase flowed continuously at the top; the interface between the phases was usually wavy, the waves rarely touched the top of the pipe wall, and the averaged $\varepsilon_{(L)}$ value was 0.311. The stratified flow pattern began when the pipe bottom was occupied by the liquid phase below its centreline, with a smooth interface between the two phases, as represented in Figure 6i. The wavy interface between the gas/liquid phases at the pipe centreline represented the liquid waves. These waves grew bigger with time, as shown in Figure 6k. A thin green interface was observed at the top of the pipe, however, this was the artefact of a very thin interface film between the two phases, appearing at high gas velocities. This cycle was always constant as stratified flow pattern was detected by ECT. These results agreed with the results available in the literature [58]. The above snapshots from ECT experiments at different flow conditions present the superiority of applying volumetric measurement for identifying the three-dimensional complexity of flow patterns compared to camera recordings.

To further validate the measured averaged $\varepsilon_{(L)}$ obtained using the ECT technique, $\varepsilon_{(L)}$ also was recorded by TFCV technique, as the latter gave instantaneous values of $\varepsilon_{(L)}$, while the former results were average values for the period of each set. Therefore, it was necessary to plot one set of results against the other. Figure 7 shows that $\varepsilon_{(L)}$ results obtained using the ECT technique were similar to the holdup measured by a fast closing valves technique. The obtained relation between the two techniques was linear, where 70% of the data fell within ±5% deviation, 86% of the data fell within ±10% deviation, and only 14% of the data were between ±10–20%. Thus, this confirmed that the results obtained from ECT yielded reliable measurements of $\varepsilon_{(L)}$. Even though the TFCV technique was less expensive than the ECT technique, this method was used in this work only for the sake of validation of the results. It is impractical to stop the operation and disturb the flow pattern as well as the holdup in real-operation conditions using the TFCV. Despite the fact that the ECT technique is expensive, it has no effect on the flow inside the pipe so it is used to save operational time and costs [20,59,60].

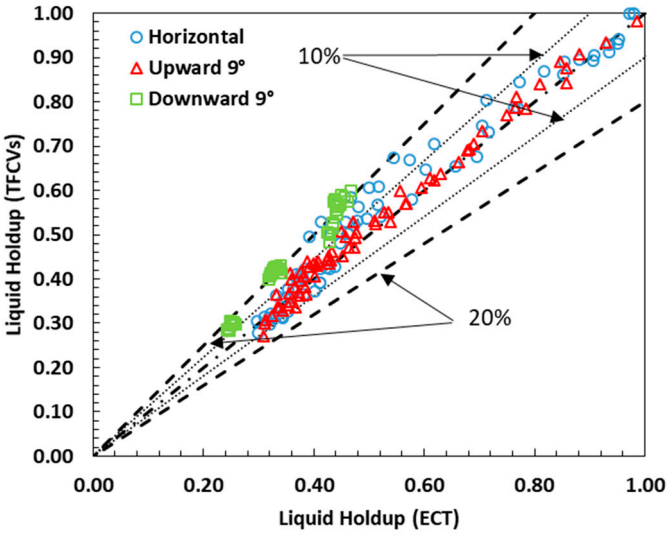

Figure 7. Validation of ECT $\varepsilon_{(L)}$ against the TFCV for all condition.

4.2. *Effect of Gas–Liquid Superficial Velocities on Liquid Holdup and Flow Pattern*

The observed flow patterns varied with pipe orientation and flow conditions. The HSCI clearly captured and helped in identifying and distinguishing the generated patterns [4,60–65]. These typical patterns were small bubble, plug, elongated bubble, slug, slug churn, stratified, stratified wavy and annular, as shown in the snapshots presented in Figure 8 for all the tested conditions.

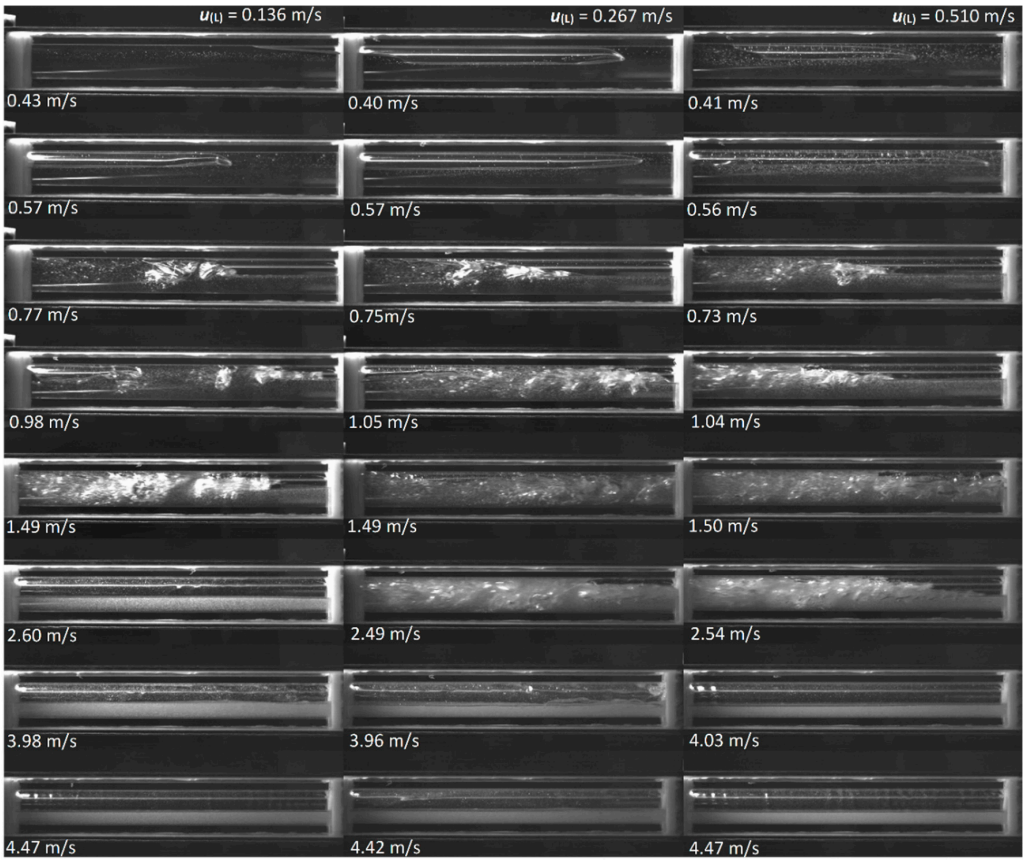

(**a**)

Figure 8. *Cont.*

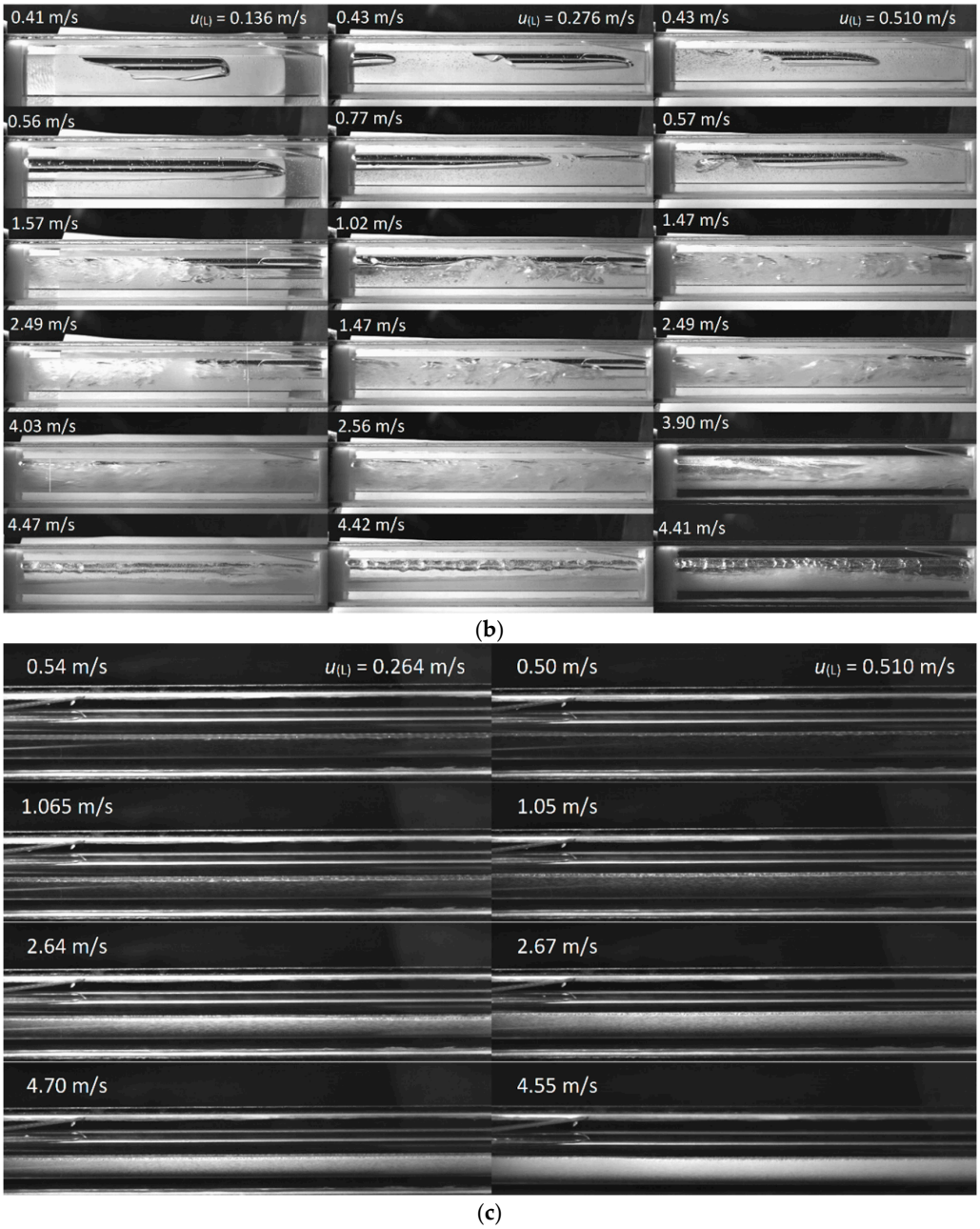

Figure 8. Snapshots from the HSCI (**a**) for horizontal inclination (0°), (**b**) for upward inclinations (9°), and (**c**) for a downward inclination (9°): at $u_{(L)}$ = 0.136, 0.264, and 0.510 m/s and varying $u_{(G)}$

Firstly, the effect of varying the liquid and gas flow rates on $\varepsilon_{(L)}$ was investigated. Figure 9a shows the horizontal case (i.e., pipe inclination angle of 0°) where $\varepsilon_{(L)}$ decreased sharply with the increase of superficial gas velocity, because the gas phase displaced the liquid phase. However, $\varepsilon_{(L)}$ increased slightly with increasing superficial liquid velocity because the liquid phase occupied a small part of the volume of the test section. The small bubble pattern had the highest $\varepsilon_{(L)}$ value, approaching 0.95 (volumetric fraction), this increased as the liquid superficial velocity was increased to reach 0.98 as a result of the mechanism of the small bubble flow pattern. As the superficial gas velocity increased, the small bubbles began to merge and to coalesce into elongated bubbles (Figure 8a at $u_{(G)}$ = 0.43–0.57 m/s). As these were larger than the small bubbles, the gas phase now occupied a higher proportion of the test section, reducing $\varepsilon_{(L)}$ value of the flow pattern. The range of $\varepsilon_{(L)}$ values was observed to be from 0.90 to 0.65 at a low superficial liquid velocity (i.e., $u_{(L)}$ = 0.136 m/s). However, at higher $u_{(L)}$, this

range started to decrease from 0.90 to 0.70 for $u_{(L)}$ = 0.276 m/s and from 0.90 to 0.82 for $u_{(L)}$ = 0.506 m/s. It is obvious from Figure 9a that the slope of the curve is proportional to the value of $\varepsilon_{(L)}$ and the gas/liquid superficial velocities, which means that it decreases as $\varepsilon_{(L)}$ decreases and that it has almost the same value as that of $\varepsilon_{(L)}$. A further small increase in superficial gas velocity causes a transition from elongated bubbles to liquid slug flow (Figure 8a at $u_{(G)}$ = 0.77–1 m/s).

Figure 9a (i.e., pipe inclination angle of 0°) and Figure 9b (i.e., upward pipe inclination angle of 9°) depict the flow pattern behaviour. Accompanying these flow patterns is the sharp drop in the curve which represents the relationship between the gas and liquid superficial velocities, $\varepsilon_{(L)}$. The flow pattern becomes steady as the slope approaches zero and has a value between 0.57 (Figure 9a) and 0.54 (Figure 9b). This kind of flow pattern can be counted as critical in both horizontal and upward inclined conditions. The liquid slug flow pattern starts to appear at a $\varepsilon_{(L)}$ value of 0.58–0.60 at a low superficial liquid velocity in both of these cases (Figure 8a,b) at $u_{(G)}$ = 0.77–1 m/s). A further increase of superficial liquid velocity causes $\varepsilon_{(L)}$ values to increase. The slug starts to disappear when the $\varepsilon_{(L)}$ value reaches 0.46 in the horizontal case (Figure 8a at $u_{(G)}$ = 1–1.50 m/s). However, in the upward case it disappears at 0.37 (Figure 8b at 1 m/s ≤ $u_{(G)}$ ≥ 2.50 m/s). Concerning both cases, higher superficial liquid velocity led to a greater increase in $\varepsilon_{(L)}$ value.

The value of $\varepsilon_{(L)}$ reduced as the superficial gas velocity increased, and the flow pattern started to change from liquid slug to slug–churn (Figure 8a at 1.50 m/s < $u_{(G)}$ < 2.50 m/s and Figure 8b at 2.49 m/s < $u_{(G)}$ < 4 m/s), when the value of $\varepsilon_{(L)}$ was between 0.43 (Figure 9a) and 0.36 (Figure 9b). A further increase in superficial gas velocity induced the stratified flow pattern in the horizontal case and $\varepsilon_{(L)}$ became constant at a low superficial liquid velocity (Figure 8a at 2.50 m/s ≤ $u_{(G)}$ < 4 m/s). However, it increased as the superficial liquid velocity increased. Regarding the horizontal case (Figure 9a), the annular flow pattern appeared only at the highest superficial gas velocities (Figure 8a at $u_{(G)}$ ≥ 4 m/s). The values of $\varepsilon_{(L)}$ in this case were almost identical to those for the stratified flow pattern and the slope of the curve was almost zero.

A comparison of Figure 9a with Figure 9b shows that the curve of the values of $\varepsilon_{(L)}$ was approximately similar for the horizontal and upward inclined pipe conditions and that the intermittent flow patterns (small bubble, plug, elongated bubble, and slug) had a major influence on the values of $\varepsilon_{(L)}$ (i.e., between $u_{(G)}$ = 0.30 m/s to 1.25 m/s and $u_{(G)}$ = 0.30 m/s to 2.70 m/s for horizontal and upward inclined pipe, respectively). When chaotic flow patterns (slug-churn) began to appear at $u_{(G)}$ = 1.25 m/s to $u_{(G)}$ = 2.50 m/s (i.e., for the horizontal case Figure 9a) and $u_{(G)}$ = 2.90 m/s to $u_{(G)}$ = 4 m/s (i.e., for the upward inclined pipe Figure 9b), $\varepsilon_{(L)}$ became minimally affected by changes in superficial gas velocity and flow patterns. A further increase in the superficial gas velocity yielded an annular flow pattern at $u_{(G)}$ = 4 m/s to $u_{(G)}$ = 5 m/s, leading to an almost constant value of holdup.

During the downward inclination condition (Figure 9c), the stratified flow pattern was dominant (Figure 8c). This could be attributed to the dominant effect of the gravity force. The value $\varepsilon_{(L)}$ was approximately constant, with a slope of zero in all cases; similar observations were reported by Xu [66]. Thus, the diamond shaped symbol represents a stratified flow pattern for all the three curves. The $\varepsilon_{(L)}$ value was unaffected by changes in superficial gas velocity, but strongly affected by increasing the superficial liquid velocity. Thus, $\varepsilon_{(L)}$ was found to be proportional to the superficial liquid velocity. Seen at superficial liquid velocities of 0.135 m/s, 0.276 m/s and 0.506 m/s, the corresponding averaged $\varepsilon_{(L)}$ values were 0.25, 0.34 and 0.45, respectively.

Such changes from horizontal (0°) to upward (+9°) inclination led to the disappearance of the stratified and stratified wavy flow patterns, as shown in Figure 9a,b, also as shown in the HSCI (Figure 8a,b). Occurring at almost the same operating condition, however at a different inclination, it was seen that a stratified wavy pattern appeared in the horizontal condition (Figure 8a at $u_{(G)}$ = 4.03 m/s and $u_{(L)}$ = 0.510 m/s), while transition from slug-churn to annular appeared on the upward condition (Figure 8b at $u_{(G)}$ = 3.90 m/s and $u_{(L)}$ = 0.510 m/s). Also, at almost the same operating condition, however, at a different inclination, we can see that slug-churn to stratified wavy appeared in the horizontal condition (Figure 8a at $u_{(G)}$ = 2.61 m/s and $u_{(L)}$ = 0.136 m/s), while slug flow appeared

on the upward condition (Figure 8b at $u_{(G)}$ = 2.49 m/s and $u_{(L)}$ = 0.136 m/s). Occurring at all gas–liquid velocity combinations, changing from horizontal (0°) to downward (−9°) inclination only showed a stratified flow pattern, as shown in Figure 9c, also as shown in the HSCI Figure 8c.

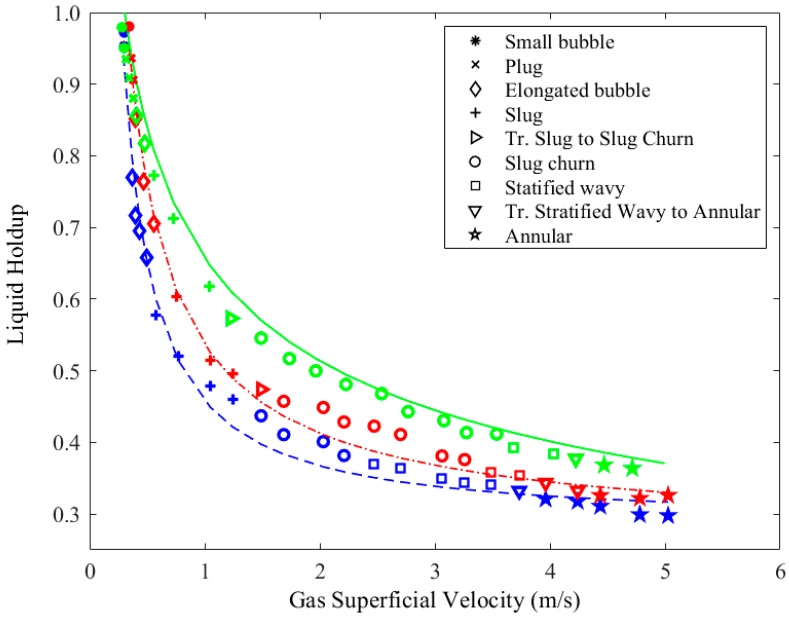

(**a**)

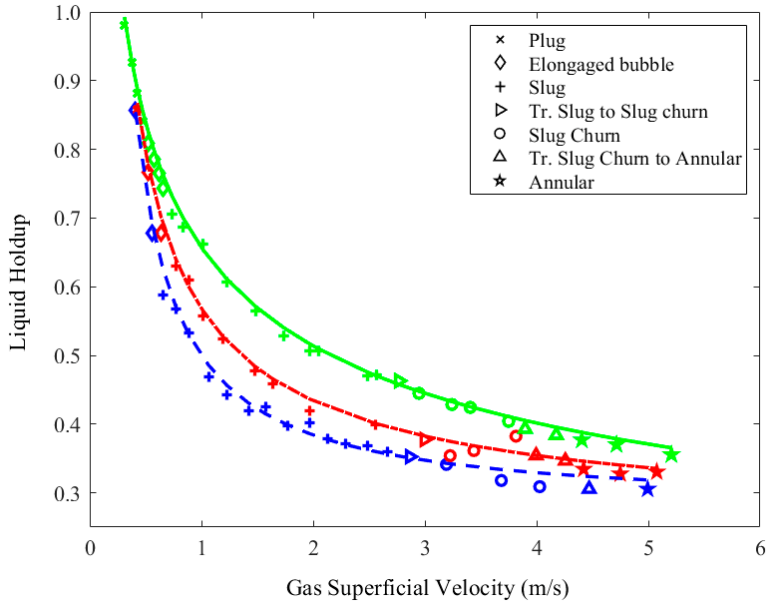

(**b**)

Figure 9. *Cont.*

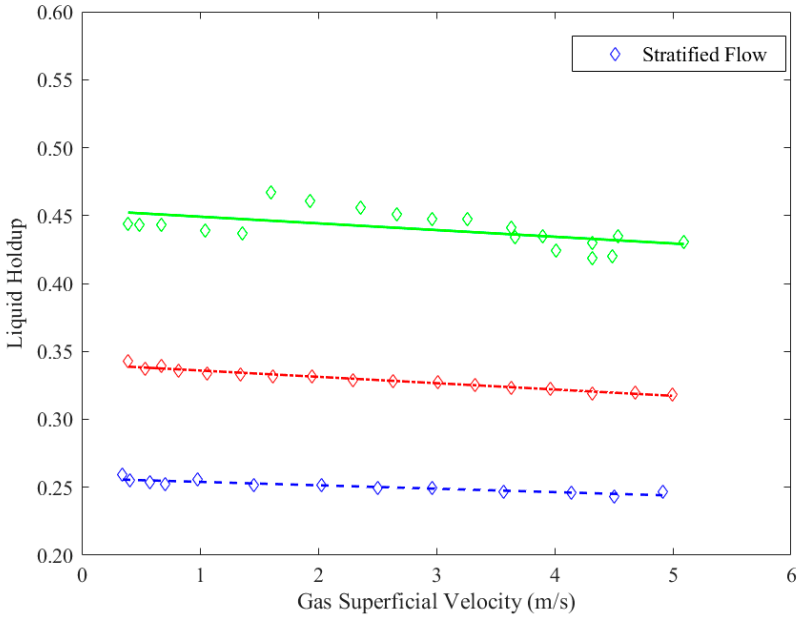

(**c**)

Figure 9. The relationship between $\varepsilon_{(L)}$ and flow pattern, based on superficial phase velocity coordinates ($u_{(L)}$: Blue: 0.135 m/s, Red: 0.276 m/s and Green: 0.506 m/s), (**a**) at pipe inclination angle of 0°, (**b**) at upward pipe inclination angle of 9°, and (**c**) at downward pipe inclination angle of 9°.

4.3. Predicting the Liquid Holdup

The proposed correlations (i.e., Equations (11) and (12) where validated against 551 data points obtained from the ECT and the TFCV in this work, and the data that can be extracted from the literature (see Table 1), the predictions are shown in Figure 10a and the residual evaluations are shown in Figure 10b.

Table 1. Data used to validate the proposed correlations.

Authors	Apparatus/Inclination	Liquid/Gas Phases	Size	No. of Data
This work	Horizontal and 9° Upward	Mineral oil (850 kg/m^3)/Air	d_{in} = 3.60 cm	282
Minami and Brill (1987) [53]	Horizontal	Kerosene (790–805 kg/m^3)/Air Water (999.65 kg/m^3)/Air	d_{in} = 7.793 cm	114
Abdul–Majeed (1996) [51]	Horizontal	Kerosene (790–805 kg/m^3)/Air	d_{in} = 5.08 cm	55
Abdul–Majeed (2000) [35]	Horizontal	Heavy oil (1000 kg/m^3)/Air	d_{in} = 5.10 cm	17
Baba et al., (2018) [25]	Horizontal	Mineral oil-CYL-680 (918 kg/m^3)/Air	d_{in} = 7.62 cm	55
Gokcal et al., (2008) [52]	Horizontal	Oil (889 kg/m^3)/Air	d_{in} = 5.08 cm	28
		Total No. Of Data Point		551

Regarding Equation (11), approximate $\varepsilon_{(L)}$ between the values of 0.09–0.90, the proposed empirical correlation predicted well the experimental measured values; the majority of the data obtained from ECT and TFCV (i.e., 88%) falls within ±15%. The remaining prediction fell slightly above ±15% and less than ±20%. Also, Equation (11) predicted the data obtained from the literature with acceptable accuracy, as shown in Figure 10. Generally, the predicted values fell within the empirical correlation's accepted accuracy range. Regarding Equation (12) the $\varepsilon_{(L)}$ approximate was between the values of 0.0082–0.275. Similarly, Equation (12) predicted well the experimental measured values. It is worth noting that both equations could not predict the downward inclination results, this is because gravity influenced the flow pattern as well as $\varepsilon_{(L)}$ more than the gas–liquid superficial velocities, as shown in Figure 9c where almost constant $\varepsilon_{(L)}$ was observed.

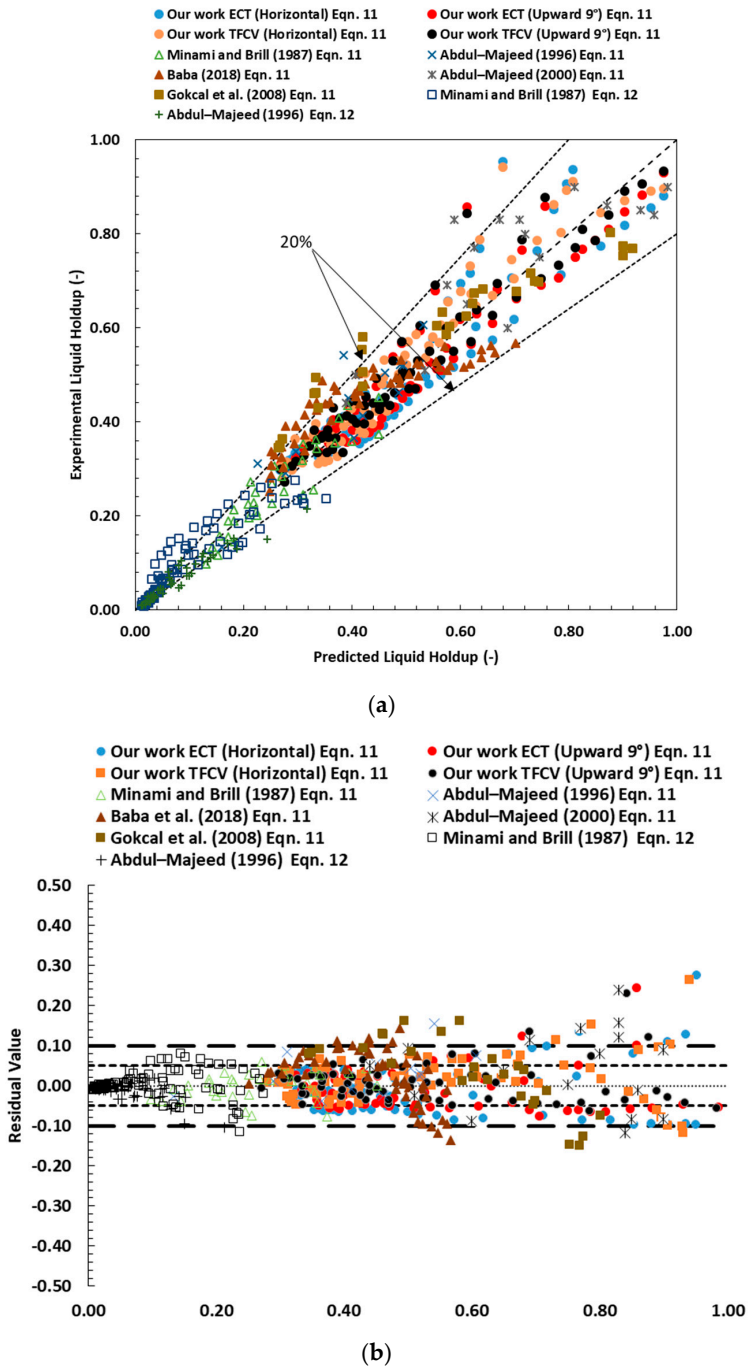

Figure 10. Equations (11) and (12): (**a**) predicted $\varepsilon_{(L)}$ against the experimental values, and (**b**) residuals of the predicted $\varepsilon_{(L)}$-(y-axis) vs. $\varepsilon_{(L)}$-(x-axis).

The proposed correlation in this work was tested against some correlations reported in the literature, as shown in Figure 11a. It is very clear that the proposed correlation in this work predicted with higher accuracy the experimental values when compared with the other correlation predictions. Also, to further test the performance of Equations (11) and (12) statistically, the residuals, average percentage error (APE), absolute average percentage error (AAPE), and the standard deviation (SD) of the predicted values were obtained. It can be seen in Figure 11b, the residual of the predicted values using the proposed correlations distribute closely around the value of zero, indicating a good agreement between the prediction results and the experimental data, while there were large discrepancies with some of the correlations that were used from the literature, which pronounced itself as scattered points.

The APE, AAPE and SD values were −1.40, 9.50, 11.46 and 8.90, 25.90, 31.20 for Equations (11) and (12), respectively. The statistical values were very low when compared with statistical values of other existing correlations, as shown in Table 2, indicating good predications. The values of all $\varepsilon_{(L)}$ are averaged values and fluctuated over time, thus, the measured SD values experimentally were in close agreement with the calculated values. This indicates that the deviation of the proposed correlation is within the experimentally measured deviation due to the continuous fluctuation of $\varepsilon_{(L)}$ (at each specific operating condition). The proposed empirical correlations were validated for the following ranges, Equation (11) for $u_{(G)}$= 0.105–20 m/s,$u_{(L)}$ = 0.0018–1.829 m/s, $u_{(G)}/u_{(L)}$ = 0.60–301.2, and $\rho_{(G)}/\rho_{(L)}$ = 0.0012–0.0015, and Equation (12) for $u_{(G)}$ = 1.56–16.6 m/s, $u_{(L)}$ = 0.00186–0.95 m/s, $u_{(G)}/u_{(L)}$ = 6.55–2564, and $\rho_{(G)}/\rho_{(L)}$ = 0.0012–0.0015.

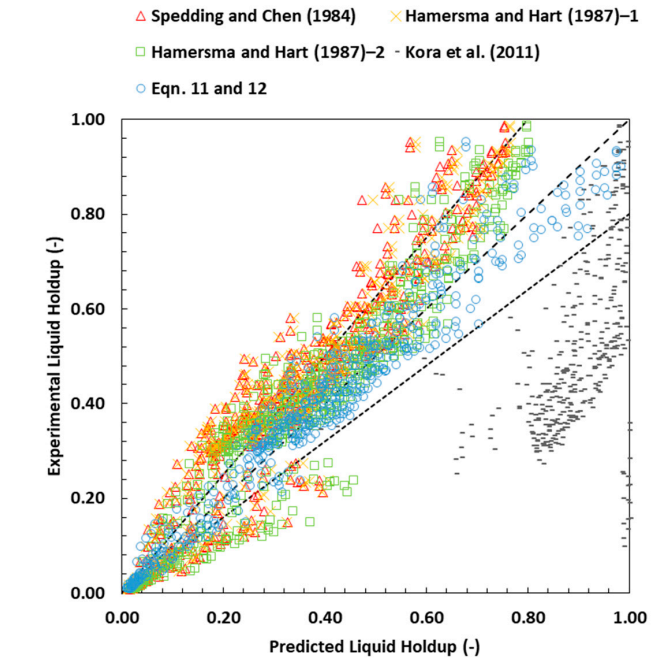

(**a**)

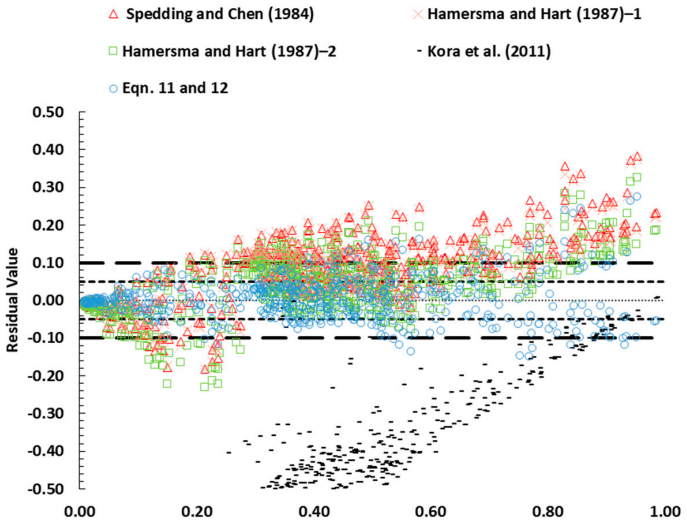

(**b**)

Figure 11. (**a**) the predicted values from Equations (11) and (12) against the correlations available in the literature and (**b**) Residuals of the predicted $\varepsilon_{(L)}$-(*y*-axis) vs. $\varepsilon_{(L)}$-(*x*-axis) using Equations (11) and (12) and the correlations available in the literature.

Table 2. Evaluation of the proposed correlation and the correlations from the literature.

Empirical Correlation	APE	AAPE	SD	Criteria	System	Gas/Liquid	Flow Type Covered	Inclination
Spedding & Chen (1984) [32,33]	−8.99 (44.09)	29.50 (49.25)	35.70 (40.04)	$\varepsilon_{(L)} \leq 0.20$	Low liquid holdup	Air/water	Annular, stratified and stratified wavy	Horizontal and vertical
Hamersma & Hart (1987)-1 [33,34]	−9.24 (40.25)	28.15 (45.63)	34 (38.57)	$\varepsilon_{(L)} \leq 0.04$	Low liquid holdup	Air/water	Stratified wavy and annular	Horizontal
Hamersma & Hart (1987)-1 [33,34]	4.15 (67.33)	27.55 (70.46)	40.45 (45.50)	$\varepsilon_{(L)} \leq 0.04$	Low liquid holdup	Air/water	Stratified wavy and annular	Horizontal
Hart et al. (1989) [33]	72.7 (104.67)	73.15 (105)	49.51 (72.37)	$\varepsilon_{(L)} \leq 0.06$	Low liquid holdup	Air/water	Stratified wavy and annular	Horizontal
Abdul–Majeed (2000) [35]	L.E. [a]	L.E. [a]	L.E. [a]	$0.2 < \varepsilon_{(L)} \leq 1$	High liquid holdup	Air/Heavy oil	Slug	Horizontal and Upward
Gomez et al., (2000) [36,42]	L.E.	L.E.	L.E.	$0.4 < \varepsilon_{(L)} \leq 1$	High liquid holdup	Air/kerosene Air/water Air/oil Nitrogen/diesel	Slug	Horizontal and Upward (50° and 90°)
Ishii (1977) [37,38]	−2.78	18.72	32.72	$0.4 < \varepsilon_{(L)} \leq 1$	High liquid holdup	N/A	Slug-churn	N/A
Bestion (1990) [38,39]	46.34	49.05	78.93	N/A	Used by research to predict high liquid holdup [38]	N/A	N/A	N/A
Al–Safran et al., (2015) [41,42]	L.E.	L.E.	L.E.	$0.6 < \varepsilon_{(L)} \leq 1$	High liquid holdup	Air/mineral oil	Slug	Horizontal
Kora et al., (2011) [40,42]	106.5	106.5	101	$0.8 < \varepsilon_{(L)} \leq 1$	High liquid holdup	Air/High viscosity oil	Slug	Horizontal
Our work Equation (11)	−1.40	9.50	11.46	$0.1 < \varepsilon_{(L)} \leq 0.986$	High liquid holdup	Air/Water Air/Kerosene Air/Heavy oil Air/Mineral oil Air/oil	Bubble, Elongated Bubble, slug and slug-churn	Horizontal and Upward (9°)
Our work Equation (12)	8.9	25.90	31.20	$0.0082 < \varepsilon_{(L)} \leq 0.275$	Low liquid holdup	Air/Water Air/Kerosene Air/Heavy oil Air/Mineral oil Air/oil	Annular, stratified and stratified wavy	Horizontal and Upward (9°)

L.E.: Large Error, [a] also large error for this correlation observed here [25,67,68], () using low liquid holdup.

Considering the above results for gas–liquid multiphase flow, the viscous forces had little influence, since the difference in viscosity between the liquid used and the gas was very high. However, what should be considered is the inertial forces, since it was the dominant force on gas–liquid multiphase flow [43]. This was evident on the correlations which had viscosity factor as a variable, such the following correlations (see Table 2, [33,35,36,40–42]). All correlations which used viscosity as a variable gave less accurate predictions. To contrast, correlations such as the one proposed here and developed by Spedding and Chen (1984), by Hamersma and Hart (1987), Bestion (1990) and Ishii (1977) had no viscosity as a variable and these correlation predictions of the experimental $\varepsilon_{(L)}$ were characterized by low uncertainty [32–34,37–39]. Regarding the pipe inclination, the correlation in this work was developed using the data obtained from horizontal and upward (9°) pipe inclinations. Therefore, it had an integral ability to predicts $\varepsilon_{(L)}$ within these values. Some of the correlations such as the Abdul–Majeed (2000) correlation [35] (i.e., developed for slug flow) had a factor for the inclination angle, however, such a factor overestimated/underestimated the prediction of the actual $\varepsilon_{(L),}$ as shown in this study (Figure 11) and by Baba et al., (2018) [25].

Additionally, regarding the transition region, Figure 5 showed that Equation (11) could predict well high $\varepsilon_{(L)}$ and as low as 0.13 while, on the other hand, Equation (12) predicted well very low $\varepsilon_{(L)}$ systems and as high as 0.26. Viewing Figure 5, it can be seen that there are two distinct lines. The line which is characterised by the presence of high to mid $\varepsilon_{(L)}$ values (which represent a typical multiphase system where the liquid occupied most of the volume), and a line at which the overall $\varepsilon_{(L)}$ dropped to a very low value and the system did not represent a multiphase flow system because the values were nearly zero (the system's volume was occupied mostly by gas). The clear overlap between the two lines (i.e., red line), represents the transition between a high liquid volume fraction system to a more chaotic and very low liquid volume fraction system (i.e., very high gas volume fraction). The $\varepsilon_{(L)}$ in this region was in the range between the value of 0.13–0.35. It is believed that in many situations where chaotic conditions occur there is a buffer region for transitioning between one model to another, and the fluid mechanics field is full of such phenomena. It is hypothesized that this transition occurs in the transition region of different flow patterns. This analysis is proven by the observed trends where there is a transition between the low $\varepsilon_{(L)}$ associated with certain flow patterns and high $\varepsilon_{(L)}$ associated with other flow patterns.

After further analysis, it is believed that this transition region is characterized by high $\varepsilon_{(L)}$ fluctuations and a high power spectrum density (PSD) of the $\varepsilon_{(L)}$ fluctuation. The uncertainty of predicting the experimental results is very high, especially if it has a very low $\varepsilon_{(L)}$ value. Therefore, there is no correlation that can give an accurate prediction of $\varepsilon_{(L)}$ in this transition region. The reason can be attributed to the fact that, in this region, $\varepsilon_{(L)}$ fluctuation is very high due to movement from high (i.e., bubble, elongated bubble and slug) and medium (slug and slug-churn) $\varepsilon_{(L)}$ to very low $\varepsilon_{(L)}$ (stratified, annular and system) that is more dominated by high gas phase, see ([51,53]). Seen in our system, the transition happened just before the region identified in Figure 5 above, because it is system-dependent and it had a relatively high $\varepsilon_{(L)}$ (i.e., 0.35) at $u_{(G)}$ = 1.49 m/s for the horizontal case. However, regarding other works, the transition happened at a relatively lower $\varepsilon_{(L)}$ that also was characterized by high fluctuation, thus the uncertainty in that region was high still. As soon as the annular flow was reached, the fluctuation dropped and it pronounced itself as low PSD, as shown in Figure 12. This transition region also can be further investigated in future work.

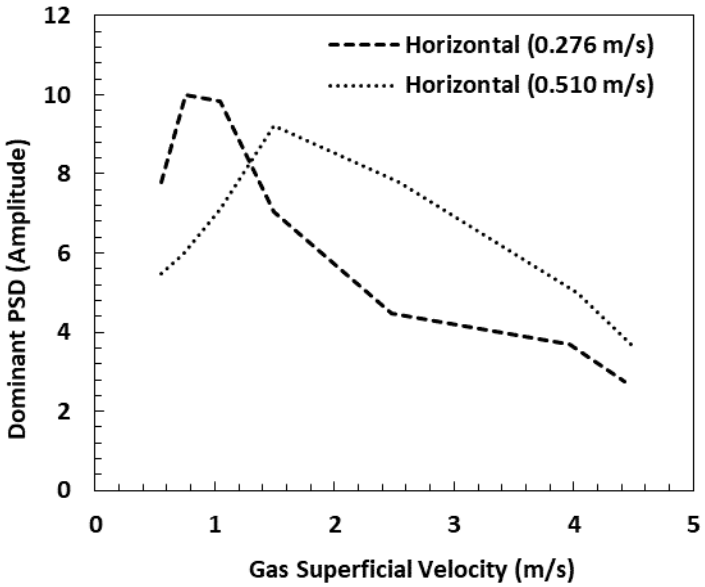

Figure 12. The max amplitude of PSD as a function of the superficial gas velocity.

5. Conclusions

Examination of two-phase gas/liquid flow was performed at three pipe inclinations in an experimental flow rig, using an eight-electrode capacitance sensor, an HSCI and TFCV to measure $\varepsilon_{(L)}$. Various flow patterns were induced by controlling gas and liquid flow rates. Superficial liquid velocity was kept constant at certain values while the superficial gas velocity was varied. The instantaneous ECT readings for various flow patterns were observed and were in agreement with high-speed camera observations. During the horizontal and upward inclined pipe conditions, intermittent flow patterns had a major influence on the value of $\varepsilon_{(L)}$ then, when chaotic (slug-churn) flow patterns began to appear, $\varepsilon_{(L)}$ became minimally affected by changes in superficial gas velocity and in flow patterns. Further increases in superficial gas velocity induced the annular flow pattern and holdup values became almost constant. During the downward pipe condition, stratified flow was the dominant pattern observed and $\varepsilon_{(L)}$ remained almost constant when superficial gas velocity was varied. However, superficial liquid velocity had a positive influence on $\varepsilon_{(L)}$ values.

Regardless of the inclination condition, the intermittent flow patterns were found to have the strongest influence on $\varepsilon_{(L)}$. To contrast, the stratified and annular flow patterns had minimal effects on the value of $\varepsilon_{(L)}$. Average $\varepsilon_{(L)}$ measured by the ECT sensor was found to match the instantaneous values obtained by the fast-closing valve method, confirming the validity of using ECT sensors for gas/oil $\varepsilon_{(L)}$ measurements. The utilization of the ECT technique proved to be beneficial when investigating the effect of varying the flow rate of the gas and the liquid on the induced $\varepsilon_{(L)}$ and its corresponding flow patterns. The obtained tomography images aided in understanding (a) different flow pattern internal behavior and (b) the interfaces between the gas and liquid phases as a function of superficial velocities and $\varepsilon_{(L)}$.

An empirical correlation to predict the average $\varepsilon_{(L)}$ was developed. The correlation was derived based on dimensionless quantities, namely, the ratio of the gas-to-liquid superficial velocities and gas-to-liquid density ratio. The predictions of the proposed empirical correlation were with accepted accuracy, where 88% of the predicted data were within ±5–15%, and 98% of the data were within ±5–20% of the actual $\varepsilon_{(L)}$ that was measured using two independent measuring techniques (i.e., ECT and TFCV). The correlations were validated against the reported experimental results and the existing correlations in the literature and showed higher prediction accuracy and fewer uncertainties.

Author Contributions: Conceptualization, Z.A. and F.M.A.-A.; Formal analysis, Z.A., F.M.A.-A., Y.A.A. and O.Y.A.; Funding acquisition, F.M.A.-A.; Investigation, Z.A., F.M.A.-A. and Y.A.A.; Methodology, Z.A., F.M.A.-A., Y.A.A. and O.Y.A.; Supervision, O.A.A. and O.Y.A.; Validation, Z.A., F.M.A.-A. and Y.A.A.; Visualization, F.M.A.-A. and Y.A.A.; Writing—original draft, Z.A., F.M.A.-A., Y.A.A., O.A.A. and O.Y.A.; Writing—review & editing, Z.A., F.M.A.-A., Y.A.A., O.A.A. and O.Y.A.; Correlation development, Y.A.A., Z.A. (Note: the first three authors contributed equally). All authors have read and agreed to the published version of the manuscript.

Funding: This work was fully funded by King Abdulaziz City for Science and Technology (KACST), grant N.: 34-997.

Acknowledgments: The author (i.e., Yusif A. Alghamdi) extends his appreciation to Deputy of Research and Innovation DRI-MOE at the Kingdom of Saudi Arabia for the Postdoctoral Fellowship Program (PFP), also acknowledge the Deanship of Scientific Research at King Saud University (KSU) for their support.

Conflicts of Interest: The authors declare no conflict of interest. The funders had no role in the design of the study; in the collection, analyses, or interpretation of data; in the writing of the manuscript, or in the decision to publish the results.

Nomenclature

Symbols	
d_{in}	internal pipe diameter (mm)
$u_{(\text{G})}$	gas superficial velocity (m/s)
$u_{(\text{L})}$	liquid superficial velocity (m/s)
E	permittivity (-)
n	number of data points (-)
Greek letter	
$\rho_{(\text{G})}$	gas density (m^3/s)
$\rho_{(\text{L})}$	liquid density (m^3/s)
$\varepsilon_{(\text{L})}$	liquid holdup (-)
$\mu_{(\text{L})}$	liquid viscosity (Pa s)
$\mu_{(\text{G})}$	gas viscosity (Pa s)
Abbreviations	
HSCI	high speed camera images
ECT	electrical capacitance tomography
ERT	electrical resistance tomography
EIT	electrical inductance tomography
LBP	linear back projection
PE	percentage error
APE	average percentage error
AAPE	absolute average percentage error
SD	standard deviation
TFCV	two fast closing valves
Subscripts	
L	liquid
G	Gas

Appendix A

$$PE = \frac{\varepsilon_{(predicted)} - \varepsilon_{(measured)}}{\varepsilon_{(measured)}} \times 100$$

$$APE = \frac{\sum_{i=1}^{n} PE_i}{n}$$

$$APE = \frac{\sum_{i=1}^{n} |PE_i|}{n}$$

$$SD = \left[\frac{n \sum_{i=1}^{n} (PE_i)^2 - \left(\sum_{i=1}^{n} PE_i \right)^2}{n^2} \right]^{0.5}$$

Table A1. Examples of experimental operating conditions and $\varepsilon_{(L)}$ from ECT and two fast closing valve (TFCV) measurements.

No. Data Point	$u_{(G)}$	$u_{(L)}$	ECT	TFCV	No. Data Point	$u_{(G)}$	$u_{(L)}$	ECT	TFCV	No. Data Point	$u_{(G)}$	$u_{(L)}$	ECT	TFCV
	m/s	m/s	$\varepsilon_{(L)}$	$\varepsilon_{(L)}$		m/s	m/s	$\varepsilon_{(L)}$	$\varepsilon_{(L)}$		m/s	m/s	$\varepsilon_{(L)}$	$\varepsilon_{(L)}$
Horizontal														
1	0.295	0.136	0.972	-	26	0.344	0.274	0.980	-	50	0.278	0.507	0.979	-
2	0.303	0.136	0.953	0.941	27	0.360	0.274	0.936	0.911	51	0.303	0.507	0.951	0.931
3	0.368	0.136	0.769	0.788	28	0.377	0.274	0.906	0.893	52	0.319	0.507	0.935	0.930
4	0.401	0.136	0.717	0.732	29	0.401	0.267	0.853	0.862	53	0.344	0.507	0.908	0.906
5	0.434	0.135	0.695	0.677	30	0.467	0.274	0.764	0.786	54	0.377	0.507	0.881	0.896
6	0.491	0.136	0.658	0.656	31	0.557	0.269	0.705	0.745	55	0.410	0.511	0.855	0.890
7	0.573	0.136	0.578	0.580	32	0.754	0.269	0.603	0.647	56	0.475	0.507	0.817	0.870
8	0.770	0.136	0.521	0.542	33	1.048	0.265	0.516	0.568	57	0.557	0.511	0.773	0.845
9	0.983	0.136	0.479	0.532	34	1.244	0.274	0.496	0.537	58	0.729	0.512	0.713	0.803
10	1.244	0.136	0.461	0.503	35	1.491	0.267	0.473	0.522	59	1.040	0.511	0.618	0.704
11	1.491	0.136	0.438	0.428	36	1.686	0.274	0.457	0.530	60	1.228	0.507	0.573	0.669
12	1.686	0.136	0.411	0.391	37	2.030	0.274	0.449	0.480	61	1.491	0.509	0.546	0.673
13	2.030	0.136	0.401	0.371	38	2.210	0.274	0.429	0.423	62	1.736	0.507	0.517	0.609
14	2.210	0.136	0.382	0.366	39	2.474	0.267	0.423	0.425	63	1.965	0.507	0.500	0.605
15	2.605	0.137	0.370	0.397	40	2.702	0.274	0.411	0.391	64	2.227	0.507	0.481	0.562
16	2.702	0.136	0.364	0.373	41	3.062	0.274	0.381	0.401	65	2.539	0.507	0.468	0.585
17	3.062	0.136	0.350	0.358	42	3.258	0.274	0.376	0.411	66	2.767	0.507	0.443	0.570
18	3.258	0.136	0.344	0.313	43	3.488	0.274	0.359	0.358	67	3.078	0.507	0.430	0.502
19	3.488	0.136	0.342	0.314	44	3.733	0.274	0.354	0.326	68	3.275	0.507	0.414	0.530
20	3.733	0.136	0.332	0.363	45	3.965	0.267	0.344	0.352	69	3.537	0.507	0.412	0.423
21	3.981	0.137	0.321	0.298	46	4.241	0.274	0.333	0.318	70	3.684	0.507	0.393	0.495
22	4.241	0.136	0.318	0.311	47	4.423	0.268	0.326	0.315	71	4.030	0.507	0.384	0.423
23	4.472	0.137	0.311	0.315	48	4.781	0.274	0.322	0.321	72	4.224	0.507	0.377	0.396
24	4.781	0.136	0.299	0.279	49	5.027	0.274	0.326	0.311	73	4.472	0.511	0.368	0.412
25	5.027	0.136	0.298	0.304						74	4.716	0.507	0.364	0.376
										75	4.994	0.507	0.354	0.378
Upward 9°														
76	0.410	0.135	0.857	0.843	97	0.429	0.268	0.858	0.877	117	0.311	0.507	0.986	0.983
77	0.557	0.136	0.678	0.690	98	0.524	0.274	0.766	0.787	118	0.377	0.507	0.930	0.933
78	0.655	0.136	0.595	0.605	99	0.639	0.274	0.682	0.694	119	0.426	0.506	0.882	0.907
79	0.770	0.131	0.568	0.570	100	0.770	0.277	0.630	0.638	120	0.475	0.507	0.847	0.890
80	0.884	0.136	0.539	0.530	101	0.884	0.274	0.618	0.623	121	0.524	0.507	0.810	0.840
81	1.065	0.133	0.475	0.492	102	1.016	0.277	0.557	0.600	122	0.573	0.506	0.785	0.785
82	1.228	0.136	0.452	0.453	103	1.195	0.274	0.527	0.550	123	0.622	0.507	0.767	0.810
83	1.424	0.136	0.424	0.445	104	1.474	0.276	0.478	0.505	124	0.655	0.507	0.750	0.771
84	1.573	0.138	0.431	0.442	105	1.638	0.276	0.458	0.495	125	0.737	0.507	0.706	0.733
85	1.768	0.136	0.401	0.407	106	1.965	0.274	0.426	0.452	126	0.835	0.507	0.690	0.704
86	1.965	0.136	0.405	0.430	107	2.556	0.276	0.400	0.435	127	1.016	0.509	0.662	0.665
87	2.129	0.136	0.384	0.383	108	2.996	0.274	0.382	0.406	128	1.228	0.507	0.610	0.627
88	2.292	0.136	0.372	0.370	109	3.226	0.274	0.357	0.413	129	1.491	0.509	0.565	0.570
89	2.490	0.134	0.374	0.362	110	3.438	0.274	0.366	0.335	130	1.736	0.507	0.535	0.550
90	2.669	0.136	0.364	0.383	111	3.815	0.274	0.386	0.365	131	1.965	0.507	0.510	0.531
91	2.865	0.136	0.357	0.349	112	3.997	0.273	0.354	0.342	132	2.047	0.507	0.512	0.525
92	3.193	0.136	0.343	0.328	113	4.423	0.279	0.335	0.335	133	2.490	0.506	0.470	0.530
93	3.684	0.136	0.324	0.316	114	4.257	0.274	0.355	0.367	134	2.571	0.507	0.473	0.471
94	4.030	0.138	0.313	0.307	115	4.748	0.274	0.333	0.365	135	2.769	0.512	0.463	0.470
95	4.472	0.134	0.310	0.272	116	5.076	0.274	0.337	0.335	136	2.947	0.507	0.450	0.508
96	4.994	0.136	0.310	0.299						137	3.242	0.507	0.432	0.462
										138	3.406	0.507	0.426	0.435
										139	3.749	0.507	0.407	0.440
										140	3.899	0.509	0.393	0.427
										141	4.175	0.507	0.388	0.440
										142	4.407	0.504	0.377	0.415
										143	4.716	0.507	0.376	0.396
										144	5.207	0.507	0.360	0.398
Downward 9°														
145	0.344	0.136	0.259	0.298	158	0.393	0.264	0.343	0.413	175	0.393	0.509	0.443	0.545
146	0.410	0.133	0.255	0.297	159	0.541	0.264	0.337	0.423	176	0.491	0.511	0.443	0.572
147	0.573	0.134	0.254	0.302	160	0.672	0.264	0.340	0.430	177	0.672	0.513	0.443	0.570
148	0.704	0.134	0.252	0.302	161	0.819	0.274	0.336	0.421	178	1.048	0.507	0.438	0.580
149	0.983	0.134	0.253	0.302	162	1.065	0.264	0.334	0.423	179	1.359	0.507	0.437	0.574
150	1.458	0.134	0.251	0.302	163	1.343	0.274	0.333	0.421	180	1.605	0.507	0.467	0.599
151	2.030	0.136	0.251	0.299	164	1.622	0.265	0.332	0.428	181	1.932	0.507	0.461	0.576
152	2.506	0.134	0.249	0.305	165	1.948	0.274	0.331	0.421	182	2.359	0.509	0.456	0.583
153	2.965	0.134	0.250	0.295	166	2.292	0.274	0.329	0.426	183	2.670	0.506	0.450	0.588
154	3.569	0.136	0.247	0.286	167	2.638	0.265	0.328	0.423	184	2.949	0.507	0.445	0.563
155	4.145	0.134	0.246	0.288	168	3.013	0.274	0.327	0.421	185	3.258	0.507	0.448	0.567
156	4.505	0.133	0.243	0.285	169	3.324	0.274	0.326	0.416	186	3.635	0.507	0.441	0.556
157	4.912	0.136	0.246	0.283	170	3.635	0.274	0.323	0.411	187	3.668	0.507	0.434	0.522
					171	3.965	0.267	0.322	0.413	188	3.897	0.507	0.435	0.514
					172	4.325	0.263	0.319	0.400	189	4.011	0.507	0.424	0.504
					173	4.685	0.267	0.320	0.405	190	4.325	0.511	0.429	0.500
					174	4.994	0.274	0.318	0.400	191	4.538	0.512	0.435	0.527
										192	4.554	0.507	0.429	0.483

References

1. Wallis, G.B. *One-Dimensional Two-Phase Flow*; McGraw-Hill Book Company: New York, NY, USA, 1969.
2. Abdulkadir, M.; Hernandez-Perez, V.; Lowndes, I.; Azzopardi, B.J.; Dzomeku, S. Experimental study of the hydrodynamic behaviour of slug flow in a vertical riser. *Chem. Eng. Sci.* **2014**, *106*, 60–75. [CrossRef]
3. Soo, S. *Multiphase Fluid Dynamics*; Science Press: Beijing, China, 1990.
4. Abduvayt, P.; Manabe, R.; Arihara, N. Effects of pressure and pipe diameter on gas-liquid tow-phase flow behavior in pipelines. In Proceedings of the In SPE Annual Technical Conference and Exhibition, Denver, CO, USA, 5–8 October 2003; pp. 1567–1581.
5. Pongsiri, S.; Somchai, W. Tow-phase flow pattern maps for vertical upward gas-liquid flow in mini-gap channels. *Int. J. Multiph. Flow* **2004**, *30*, 225–236.
6. Van Hout, R.; Shemer, L.; Barnea, D. Evolution of hydrodynamic and statistical parameters of gas-liquid slug flow along inclined pipes. *Chem. Eng. Sci.* **2003**, *58*, 115–133. [CrossRef]
7. Ekberg, N.P.; Ghiaasiaan, S.M.; Abdel-Khalik, S.I.; Yoda, M.; Jeter, S.M. Gas-liquid two-phase flow in narrow horizontal annuli. *Nucl. Eng. Des.* **1999**, *192*, 59–80. [CrossRef]
8. Furukawa, T.; Fukano, T. Effects of liquid viscosity on flow pattern in vertical upward gas-liquid two phase flow. *Int. J. Multiph. Flow* **2001**, *27*, 1109–1126. [CrossRef]
9. Hewitt, G.F.; Robertson, D.N. *Studies of Two-Phase Flow Patterns by Simultaneous X-ray and Flash Photography*; Report AERE-M2159; UKAEA; Atomic Energy Research Establishment: Harwell, UK, 1969.
10. Adewumi, M.A.; Bukacek, R.F. Two-phase pressure drop in horizontal pipelines. *J. Pipelines* **1985**, *5*, 1–14.
11. Barnea, D.; Brauner, N. Hold-up of liquid in two phase intermittent flow. *Int. J. Multiph. Flow* **1985**, *11*, 43–49. [CrossRef]
12. Taitel, Y.; Barnea, D.; Dukler, A.E. Modelling flow pattern transitions for steady upward gas-liquid flow in vertical tubes. *AIChE J.* **1980**, *26*, 345–954. [CrossRef]
13. Taitel, Y.; Dukler, A.E. A model for predicting flow regime transition in horizontal and near horizontal gas liquid flow. *AIChE J.* **1976**, *22*, 47–55. [CrossRef]
14. Ismail, I.; Gamio, J.C.; Bukhari, S.F.A.; Yang, W.Q. Tomography for multi-phase flow measurement in the oil industry. *Flow Meas. Instrum.* **2005**, *16*, 145–155. [CrossRef]
15. Williams, R.A.; Beck, M.S. *Process Tomography Principle, Techniques and Applications*; Butterworth-Heinemann Ltd: Oxford, UK, 1995.
16. Bieberle, M.; Hampel, U. Evaluation of a limited angle scanned electron beam x-ray ct approach for two-phase pipe flows. *Meas. Sci. Technol.* **2006**, *17*, 2057–2065. [CrossRef]
17. Tollefesn, J.; Hammer, E. Capacitance sensor design for reducing errors in phase concentration measurements. *Flow Meas. Instrum.* **1998**, *9*, 25–32. [CrossRef]
18. Yang, W.Q.; Chondronasios, A.; Nattrass, S.; Nguyen, V.T.; Betting, M.; Ismail, I.; McCann, H. Adaptive calibration of capacitance tomography system for imaging water droplet distribution. *Flow Meas. Instrum.* **2004**, *15*, 249–258. [CrossRef]
19. Wang, G.; Ching, C.Y. Measurement of multiple gas-bubble velocities in gas-liquid flows using hot film anemometry. *Exp. Fluids* **2001**, *31*, 428–439. [CrossRef]
20. Wu, H.; Tan, C.; Dong, X.; Dong, F. Design of a conductance and capacitance combination sensor for water holdup measurement in oil–water two-phase flow. *Flow Meas. Instrum.* **2015**, *46*, 218–229. [CrossRef]
21. Sardeshpande, M.V.; Harinarayan, S.; Ranade, V.V. Void fraction measurement using electrical capacitance tomography and high speed photography. *Chem. Eng. Res. Des.* **2015**, *94*, 1–11. [CrossRef]
22. Clarke, N.N.; Rezkallah, K.S. A study of drift velocity in bubbly two-phase flow under microgravity conditions. *Int. J. Multiph. Flow* **2001**, *27*, 1533–1554. [CrossRef]
23. Xia, G.; Zhou, F.; Hu-ming, S. Two-phase slug flow in vertical and inclined tubes. *Nucl. Sci. Tech.* **1996**, *7*, 232–237.
24. Bolton, G.T.; Korchinsky, W.J.; Waterfall, R.C. Imaging Immiscible Liquid-Liquid Systems by Capacitance Tomography. *Chem. Eng. Res. Des.* **1999**, *77*, 699–708. [CrossRef]
25. Baba, Y.D.; Aliyu, A.M.; Archibong, A.-E.; Almabrok, A.A.; Igbafe, A.I. Study of high viscous multiphase phase flow in a horizontal pipe. *Heat Mass Transf.* **2018**, *54*, 651–669. [CrossRef]
26. Ramli, M.F.; Avila, H.E.L.; Sousa, F.R.d.; Tian, W.; Yang, W. Multiphase Flow Measurement by Electrical Capacitance Tomography and Microwave Cavity Resonant Sensor. In Proceedings of the 2019 IEEE

International Instrumentation and Measurement Technology Conference (I2MTC), Auckland, New Zealand, 20–23 May 2019; pp. 1–6.
27. Gamio, J.C.; Castro, J.; Rivera, L.; Alamilla, J.; Garcia-Nocetti, F.; Aguilar, L. Visualisation of gas-oil two-phase flows in pressurised pipes using electrical capacitance tomography. *Flow Meas. Instrum.* **2005**, *16*, 129–134. [CrossRef]
28. Liu, S.; Chen, Q.; Wang, H.G.; Jiang, F.; Ismail, I.; Yang, W.Q. Electrical capacitance tomography for gas-solids flow measurement for circulating fluidized beds. *Flow Meas. Instrum.* **2005**, *16*, 135–144. [CrossRef]
29. Tapp, H.S.; Peyton, A.J.; Kemsley, E.K.; Wilson, R.H. Chemical engineering applications of electrical process tomography. *Sens. Actuators B Chem.* **2003**, *92*, 17–24. [CrossRef]
30. Bangliang, S.; Zhang, Y.; Peng, L.; Yao, D.; Zhang, B. The use of simultaneous iterative reconstruction technique for electronic capacitance tomography. *Chem. Eng. J.* **2000**, *77*, 37–41. [CrossRef]
31. Reinecke, N.; Mewes, D. Multielectrode capacitance sensors for the visualisation of transient two-phase flows. *Exp. Therm. Fluid Sci.* **1997**, *15*, 253–266. [CrossRef]
32. Spedding, P.L.; Chen, J.J.J. Holdup in two phase flow. *Int. J. Multiph. Flow* **1984**, *10*, 307–339. [CrossRef]
33. Hart, J.; Hamersma, P.J.; Fortuin, J.M.H. Correlations predicting frictional pressure drop and liquid holdup during horizontal gas-liquid pipe flow with a small liquid holdup. *Int. J. Multiph. Flow* **1989**, *15*, 947–964. [CrossRef]
34. Hamersma, P.J.; Hart, J. A pressure drop correlation for gas/liquid pipe flow with a small liquid holdup. *Chem. Eng. Sci.* **1987**, *42*, 1187–1196. [CrossRef]
35. Abdul-Majeed, G.H. Liquid slug holdup in horizontal and slightly inclined two-phase slug flow. *J. Pet. Sci. Eng.* **2000**, *27*, 27–32. [CrossRef]
36. Gomez, L.E.; Shoham, O.; Taitel, Y. Prediction of slug liquid holdup: Horizontal to upward vertical flow. *Int. J. Multiph. Flow* **2000**, *26*, 517–521. [CrossRef]
37. Ishii, M. *One-Dimensional Drift-Flux Model and Constitutive Equations for Relative Motion between Phases in Various Two-Phase Flow Regimes*; Argonne National Lab., Ill: Lemont, IL, USA, 1 October 1977.
38. Choi, J.; Pereyra, E.; Sarica, C.; Park, C.; Kang, J.M. An Efficient Drift-Flux Closure Relationship to Estimate Liquid Holdups of Gas-Liquid Two-Phase Flow in Pipes. *Energies* **2012**, *5*, 5294–5306. [CrossRef]
39. Bestion, D. The physical closure laws in the CATHARE code. *Nucl. Eng. Des.* **1990**, *124*, 229–245. [CrossRef]
40. Kora, C.; Sarica, C.; Zhang, H.-q.; Al-Sarkhi, A.; Al-Safran, E. Effects of High Oil Viscosity on Slug Liquid Holdup in Horizontal Pipes. In Proceedings of the Canadian Unconventional Resources Conference, Calgary, AB, Canada, 1 January 2011; p. 15.
41. Al-Safran, E.; Kora, C.; Sarica, C. Prediction of slug liquid holdup in high viscosity liquid and gas two-phase flow in horizontal pipes. *J. Pet. Sci. Eng.* **2015**, *133*, 566–575. [CrossRef]
42. Abdul-Majeed, G.H.; Al-Mashat, A.M. A unified correlation for predicting slug liquid holdup in viscous two-phase flow for pipe inclination from horizontal to vertical. *SN Appl. Sci.* **2018**, *1*, 71. [CrossRef]
43. Farokhpoor, R.; Liu, L.; Langsholt, M.; Hald, K.; Amundsen, J.; Lawrence, C. Dimensional analysis and scaling in two-phase gas–liquid stratified pipe flow–Methodology evaluation. *Int. J. Multiph. Flow* **2020**, *122*, 103139. [CrossRef]
44. Alghamdi, Y.; Peng, Z.; Shah, K.; Moghtaderi, B.; Doroodchi, E. Predicting the solid circulation rate in chemical looping combustion systems using pressure drop measurements. *Powder Technol.* **2015**, *286*, 572–581. [CrossRef]
45. Wu, X.; Lu, H.; Wu, S. Stress analysis of parallel oil and gas steel pipelines in inclined tunnels. *Springerplus* **2015**, *4*, 659. [CrossRef]
46. Wen, Y.; Wu, Z.H.; Wang, J.L.; Wu, J.; Yin, Q.G.; Luo, W. Experimental study of liquid holdup of liquid-gas two-phase flow in horizontal and inclined pipes. *Int. J. Heat Technol.* **2017**, *35*, 713–720. [CrossRef]
47. Hanafizadeh, P.; Eshraghi, J.; Nazari, Y.; Yousefpour, K.; Akhavan Behabadi, M.A. Light Oil–Gas Two-Phase Flow Pattern Identification in Different Pipe Orientations: An Experimental Approach. *Sci. Iran* **2017**, *24*, 2445–2456. [CrossRef]
48. Goldszal, A.; Monsen, J.I.; Danielson, T.J.; Bansal, K.M.; Yang, Z.L.; Johansen, S.T.; Depay, G. Ledaflow 1D: Simulation Results With Multiphase Gas/Condensate and Oil/Gas Field Data. In Proceedings of the 13th International Conference on Multiphase Production Technology, Edinburgh, UK, 13 June 2007; p. 15.
49. Kang, C.; Jepson, W.P.; Wang, H. Flow Regime Transitions in Large Diameter Inclined Multiphase Pipelines. In Proceedings of the CORROSION 2002, Denver, CO, USA, 1 January 2002; p. 11.

50. Alghamdi, Y.; Peng, Z.; Shah, K.; Moghtaderi, B.; Doroodchi, E. A correlation for predicting solids holdup in the dilute pneumatic conveying flow regime of circulating and interconnected fluidised beds. *Powder Technol.* **2016**, *297*, 357–366. [CrossRef]
51. Abdul-Majeed, G.H. Liquid holdup in horizontal two-phase gas—Liquid flow. *J. Pet. Sci. Eng.* **1996**, *15*, 271–280. [CrossRef]
52. Gokcal, B.; Wang, Q.; Zhang, H.-Q.; Sarica, C. Effects of High Oil Viscosity on Oil/Gas Flow Behavior in Horizontal Pipes. *SPE Proj. Facil. Constr.* **2008**, *3*, 1–11. [CrossRef]
53. Minami, K.; Brill, J.P. Liquid Holdup in Wet-Gas Pipelines. *SPE Prod. Eng.* **1987**, *2*, 36–44. [CrossRef]
54. Al-Dahhan, M.H.; Khadilkar, M.R.; Wu, Y.; Duduković, M.P. Prediction of Pressure Drop and Liquid Holdup in High-Pressure Trickle-Bed Reactors. *Ind. Eng. Chem. Res.* **1998**, *37*, 793–798. [CrossRef]
55. Al-Safran, E. Prediction of Slug Liquid Holdup in Horizontal Pipes. *J. Energy Resour. Technol.* **2009**, *131*. [CrossRef]
56. Mukherjee, H.; Brill, J.P. Liquid Holdup Correlations for Inclined Two-Phase Flow. *J. Pet. Technol.* **1983**, *35*, 1003–1008. [CrossRef]
57. Jain, A.; Paul, A.R.; Aggarwal, S.K.; Mohanty, B.; Mani, B.P. A new correlation for holdup in gas-solids cyclone. In Proceedings of the 2011 international conference on Applied & Computational Mathematics, Canary Islands, Spain, 27–29 May 2011; pp. 117–126.
58. Perera, K.; Pradeep, C.; Mylvaganam, S.W. Time, R. Imaging of oil-water flow patterns by electrical capacitance tomography. *Flow Meas. Instrum.* **2017**, *56*, 23–34. [CrossRef]
59. Chen, X.; Han, Y.F.; Ren, Y.Y.; Zhang, H.X.; Zhang, H.; Jin, N.D. Water holdup measurement of oil-water two-phase flow with low velocity using a coaxial capacitance sensor. *Exp. Therm. Fluid Sci.* **2017**, *81*, 244–255. [CrossRef]
60. Salehi, S.M.; Karimi, H.; Moosavi, R.; Dastranj, A.A. Different configurations of capacitance sensor for gas/oil two phase flow measurement: An experimental and numerical study. *Exp. Therm. Fluid Sci.* **2017**, *82*, 349–358. [CrossRef]
61. Barnea, D.; Shoham, O.; Taitel, Y. Flow pattern transition for vertical downward two phase flow: Horizontal to vertical. *Chem. Eng. Sci.* **1982**, *37*, 735–740. [CrossRef]
62. Barnea, D.; Shoham, O.; Taitel, Y. Flow pattern transition for vertical downward two phase flow. *Chem. Eng. Sci.* **1982**, *37*, 741–744. [CrossRef]
63. Szalinski, L.; Abdulkareem, L.A.; Silva, M.J.D.; Thiele, S.; Beyer, M.; Lucas, D.; Perez, V.H.; Hampel, U.; Azzopardi, B.J. Comparative study of gas–oil and gas–water two-phase flow in a vertical pipe. *Chem. Eng. Sci.* **2010**, *65*, 3836–3848. [CrossRef]
64. Zhao, Y.; Yeung, H.; Zorgani, E.E.; Archibong, A.E.; Lao, L. High viscosity effects on characteristics of oil and gas two-phase flow in horizontal pipes. *Chem. Eng. Sci.* **2013**, *95*, 343–352. [CrossRef]
65. Milan, M.; Borhani, N.; Thome, J.R. Adiabatic vertical downward air–water flow pattern map: Influence of inlet device, flow development length and hysteresis effects. *Int. J. Multiph. Flow* **2013**, *56*, 126–137. [CrossRef]
66. Xu, J. Investigation on average void fraction for air/non-Newtonian power-law fluids two-phase flow in downward inclined pipes. *Exp. Therm. Fluid Sci.* **2010**, *34*, 1484–1487. [CrossRef]
67. Ibarra, R.; Nossen, J.; Tutkun, M. Holdup and frequency characteristics of slug flow in concentric and fully eccentric annuli pipes. *J. Pet. Sci. Eng.* **2019**, *182*, 106256. [CrossRef]
68. Zhao, Y.; Lao, L.; Yeung, H. Investigation and prediction of slug flow characteristics in highly viscous liquid and gas flows in horizontal pipes. *Chem. Eng. Res. Des.* **2015**, *102*, 124–137. [CrossRef]